Applied Physics Laboratory
University of Washington

1013 NE 40th Street
Box 355640
Seattle, WA 98105-6698

206-543-1300
FAX 206-543-6785
www.apl.washington.edu

August 26, 2021

To: Dr. Kyle Becker
Office of Naval Research (Code 322)
875 North Randolph Street
Arlington, VA 22203-1995

From: Dr. Peter Dahl, Principal Investigator

Subj: ONR Grant#N00014-17-1-2170, "Intensity Vector Acoustics and Mid Frequency Sonar Studies, and Experiments in Korean Coastal Waters"

Encl: (1) Final Technical Report for Subject Grant
(2) ASA Publication "Trends in low-frequency underwater noise off the Oregon coast and impacts of COVID-19 pandemic."
(3) IEEE Publication "Vector Acoustics Analysis of Time-Separated Modal Arrivals From Explosive Sound Sources During the 2017 Seabed Characterization Experiment."
(4) IEEE Publication "Range-Dependent Inversion for Seabed Parameters Using Vector Acoustic Measurements of Underwater Ship Noise."
(5) SF298 for Enclosure

Enclosure (1) is the Final Technical Report for the subject grant along with 3 presented works (2,3,4). Enclosure (5) is the SF 298 form. These documents constitute the Final Technical Report and deliverable for ONR Grant# N00014-17-1-2170.

cc: Grant & Contract Administrator, APL-UW
Office of Sponsor Programs, UW
ONR Seattle
Naval Research Laboratory
Defense Technical Information Center

Intensity Vector Acoustics and Mid Frequency Sonar Studies, and Experiments in Korean Coastal Waters

Peter H. Dahl
Applied Physics Laboratory
University of Washington
Seattle, WA 98105

26 August 2021

Final Report
Award Number N00014-17-1-2170

The technical works and presentations listed here cover research completed between 15 January 2017 and 14 April 2021, funded by the ONR grant entitled: "Intensity Vector Acoustics and Mid-Frequency Sonar Studies, and Experimental in Korean Coastal Waters."

There were two, related objectives of this ONR grant, the first more generally was to increase our understanding of the acoustic intensity vector field as it applies to shallow water propagation and reverberation. The second was to carry out two field experiments in Korea, the first completed in May 2017 however the second field trial scheduled for spring 2020 but canceled owing to Covid-19.

The start of this grant also overlapped to some extent with preparation and execution of the Seabed Characterization Experiment 2017 (SBCEX2017) experiment off New England in March 2017. Vector acoustic data that emerged from SBCEX2017 was of extremely high quality along with environmental data, relative to the field experiment in Korea. Thus, much of the effort from this grant was directed towards analysis of SBCEX2017 experimental observations. These observations originate from the instrument known as the Intensity Vector Autonomous Recorder (IVAR) deployed during SBCEX2017.

We also remark that owing to the cancellation of the 2nd field experiment in Korea in spring 2020, some funds from this grant were redirected by sponsor permission towards preparation of a pilot experiment conducted in spring 2021 involving our team to obtain vector acoustic observations further off shore from the SBEX2017 site.

Below lists several refereed published studies completed under this grant or partially supported by it. Of these, we consider three as representative of the primary technical output from this grant and a copies of these works are attached.

The papers entitled "Vector acoustic analysis of time-separated arrivals from explosive sound sources during the 2017 Seabed Characterization Experiment" (2020) and "Range-dependent inversion for seabed parameters using vector acoustic measurements of underwater ship noise" (2021), involve the IVAR system used in SBCEX2017.

In the first, a new approach is developed to evaluate vector acoustic observations of dispersed arrivals originating from SUS sources. Quantities such as depth-dependent mode speed of energy and Circularity are formed both theoretically and from experimental observations. These quantities are estimated on single-mode basis made possible by the dispersed arrivals in the data. It shown that these quantities are highly sensitive to the seabed conditions and a pathway towards inversion is discussed.

In the second, the non-dimensional quantity known as Circularity as constructed from vector intensity, is revisited using measurements of noise from a commercial ship passing by the IVAR system. As in the case of the broad band SUS data, a theoretical model for Circularity is developed but here multiple modes are included. A Bayesian framework is then applied for purposes of geoacoustic inversion.

The third study is entitled "Trends in low-frequency underwater noise off the Oregon coast and impacts of the COVID-19 pandemic" (2021) and was motivated by the emergence of Covid-19. Though not immediately linked to our other studies in vector acoustics, this study opened up a new data stream for our team made available by the Regional Cabled Array network yielding acoustic and oceanographic data gathered in the Northeast Pacific, in this case the data are from station HYS14 located 87 km offshore of Newport, OR. The detailed analysis of 6 years of underwater noise data revealed a subtle, but clearly discernible, influence of reduced shipping noise owing to scaled back economic activity caused by the worldwide COVID-19 epidemic. Furthermore, the study provided one of the clearest demonstrations of the effect of seasonal variation in shipping noise levels linked with near-surface water temperature seasonal variation.

Technical Articles based on research funded by Office of Naval Research Grant N000014-17-1-2170 for period January 2017-April 2021

Refereed Publications

1. P. H. Dahl, D. R. Dall'Osto, and M. J. Harrington, Trends in low-frequency underwater noise off the Oregon coast and impacts of the COVID-19 pandemic, ***J. Acoust. Soc. Am.***, 149, 4073-4077, June 2021.
2. P. H. Dahl and D.R. Dall'Osto, Range-dependent inversion for seabed parameters using vector acoustic measurements of underwater ship noise, ***IEEE J. Oceanic Engineering***, (currently online only) , DOI 10.1109/JOE.2021.3086880, June 2021.

3. A. G. Marusiak, N. C. Schmerr, D. N. DellaGiustina, E. C. Pettit, P. H. Dahl, B. Avenson, S. H. Bailey, V. J. Bray, N. Wagner, C. G. Carr, R. C. Weber, The Deployment of the Seismometer to Investigate Ice and Ocean Structure (SIIOS) on Gulkana Glacier, Alaska, ***Seismological Research Letters*** 91 (3), 1901-1914, 2020.
4. P. H. Dahl, A. K. Jenkins, B. Casper, S. E. Kotecki, V. Bowman, C. Boerger, D. R. Dall'Osto1, M. A. Babina, and A. N. Popper, Physical Effects of Sound Exposure from Underwater Explosions on Pacific Sardines (*Sardinops sagax*), ***J. Acoust. Soc. Am.,*** 139, 311-319, May 2020.
5. D.V. Van Komen, T. B. Neilsen, K. Howarth, D. P. Kobles and P. H. Dahl, Seabed and range estimation using a convolutional neural network, ***J. Acoust. Soc. Am.***, ***Express Letters,*** EL 403-408, May 2020.
6. P. H. Dahl and D.R. Dall'Osto, Estimation of seabed properties and range from vector acoustic observations of underwater ship noise, ***J. Acoust. Soc. Am.***, ***Express Letters,*** EL 345-350, April 2020.
7. P. H. Dahl and D.R. Dall'Osto, Vector acoustic analysis of time-separated arrivals from explosive sound sources during the 2017 Seabed Characterization Experiment, ***IEEE J. Oceanic Engineering***, 45, 131-143, 2020.
8. P. S. Wilson, D. P. Knobles, P. H. Dahl, A. R. McNeese, and M. C. Zeh, (2019). Short-range signatures of explosive sounds in shallow water used for seabed characterization, ***IEEE J. Oceanic Engineering***, 45, 1-12, 2020.
9. P. H. Dahl and D.R. Dall'Osto, On the underwater sound field from impact pile driving: Arrival structure, precursor arrivals, and energy streamlines, ***J. Acoust. Soc. Am.,*** 142, 1141-1155, Aug. 2017.

References 3 and 4 were produced with partial support from this grant with majority funding from other sources.

Conference Presentations

1. P. H. Dahl and D.R. Dall'Osto, "Vector Acoustic Properties of Underwater Sound Fields ," ICUA International Conference on Underwater Acoustics, U.K. (held virtually) (July 2020).

2. P. H. Dahl and D.R. Dall'Osto, "Vector acoustic study of ship noise during the 2017 Seabed Characterization Experiment ," Acoustical Society of America Conference, San Diego , CA (December 2019).

3. P. H. Dahl and D.R. Dall'Osto, "Vector intensity properties from a direct and reverberant field from a mid-frequency sonar in shallow water," Acoustical Society of America Conference, Victoria , B.C. (December 2018).

4. P. H. Dahl and D.R. Dall'Osto, "The rate of energy transport and direct measurements of group velocity", Acoustical Society of America Conference, Victoria , B.C. (December 2018).

5. David Knobles, Peter Dahl, David Dall'Osto, and Preston Wilson "Statistical inference approach applied to simultaneous vertical particle velocity and acoustic pressure measurements from SUS explosive sources made in the New England Mudpatch" , Acoustical Society of America Conference, Victoria , B.C. (December 2018).

6. D.R. Dall'Osto and P. H. Dahl, "Observations of resonances and anti-resonances in modal propagation over muddy sediment layer ", Acoustical Society of America Conference, Victoria , B.C. (December 2018).

7. P. H. Dahl and D.R. Dall'Osto, "Pressure and particle velocity measurements from a broad band source at ranges 1-10 km ," Acoustical Society of America Conference, Minneapolis, MN (May 2018).

8. D. R. Dall'Osto, P. H. Dahl and D.J. Tang, B. Hefner, T. Shim, "Intensity properties of the field at a fixed range from a mid-frequency sonar in shallow water", Acoustical Society of Korea meeting (presented by Dahl), (September 2017)

Graduate Student Supervision

Alex Soloway, Ph.D. completed May 2018, topic: shallow water propagation from explosive sources including Scholte wave generation and propagation.

> Thesis Title: Environmental Noise from Underwater Explosions and Impact of Seabed on Received Levels.

Alex was funded by 2-year ONR Graduate Traineeship, ending 2018, with some overlap of this grant with his time at the UW.

JASA ARTICLE

Trends in low-frequency underwater noise off the Oregon coast and impacts of COVID-19 pandemic[a)]

Peter H. Dahl,[b)] David R. Dall'Osto, and Michael J. Harrington
Applied Physics Laboratory, University of Washington, Seattle, Washington 98105, USA

ABSTRACT:
Approximately six years of underwater noise data recorded from the Regional Cabled Array network are examined to study long-term trends. The data originate from station HYS14 located 87 km offshore of Newport, OR. The results indicate that the third-octave band level centered at 63 Hz and attributable to shipping activity is reduced in the spring of 2020 by about 1.6 dB relative to the mean of the prior five years, owing to the reduced economic activity initiated by the COVID-19 pandemic. The results are subtle, as the noise reduction is less than the typical seasonal fluctuation associated with warming ocean surface temperatures in the summer that reduces mode excitation support at typical ship source depths, causing a repeated annual level change on the order of 4 dB at shipping frequencies. Seasonality of the noise contribution near 20 Hz from fin whales is also discussed. Corroboration of a COVID-19 effect on shipping noise is offered by an analysis of automatic identification system shipping data and shipping container activity for Puget Sound, over the same six-year period, which shows a reduction in the second quarter of 2020 by ∼19% and ∼17%, respectively, relative to the mean of the prior five years.
 https://doi.org/10.1121/10.0005192

(Received 30 March 2021; accepted 14 May 2021; published online 9 June 2021)

[Editor: James F. Lynch] Pages: 4073–4077

I. INTRODUCTION

The Ocean Observatories Initiative (OOI) Regional Cabled Array (RCA),[1,2] funded by the National Science Foundation, provides a constant stream of data from the seafloor and water column spanning the Juan de Fuca plate. Here, we present underwater sound data recorded at the RCA site known as Hydrate Ridge station HYS14 (Fig. 1), located on the seabed at a depth of 778 m, approximately 87 km offshore of Newport, OR (44.569° N, 125.148° W). We examine long-term trends in shipping-related underwater noise and how trends compare to recent conditions that may have been impacted by the COVID-19 pandemic.

The HYS14 hydrophone commenced data streaming on 15 January 2015, and this study incorporates all data from that point until 17 August 2020, after which the primary node (PN1B) of the RCA developed a fault that took part of the RCA infrastructure offline. (Replacement of the failed node is scheduled for summer 2021.) Station HYS14 was selected for analysis primarily because there are fewer noise producing real-time measurement systems at this station relative to other stations within the RCA system. The site is well situated within north-south coastal shipping lanes (Fig. 1) and likely to experience more distant traffic noise[3,4] associated with great-circle shipping routes connecting northwest ports (e.g., Vancouver, BC, and Seattle and Tacoma, WA) with Asian ports.

The paper is organized as follows: Sec. II describes data and processing methods in the frequency domain. Note that we use both linear and geometric averages to describe measures of central tendency in spectral and mean-square levels depending on the purpose, which will be explained. Section III provides results, including a short summary of the biophony that must be understood in the context of the noise related to shipping. Here, we also document the seasonal propagation effect for near-surface radiated shipping noise, including simple modeling that captures the trends. These two elements provide necessary background for our conclusions related to underwater noise shipping and economic impacts of COVID-19, discussed in Sec. IV and summarized in Sec. V.

II. DATA DESCRIPTION AND PROCESSING METHODS

The data were obtained through the Incorporated Research Institutions for Seismology (IRIS) network, accessing station OO, sensor HYS14. The sampling frequency is 200 Hz applied after data are low-pass filtered with a 3-dB corner frequency of about 90 Hz prior to sampling. The HYS14 hydrophone is an HTI-90-U low-frequency hydrophone manufactured by HiTech (Long Beach, MS), with effective receiving sensitivity (inclusion of gain) equal to –174 dB re V/μPa.

The basic spectral analysis revolves around the sequence of whole hours for a given day as recorded in UTC, as follows. We take the fast Fourier transform (FFT) of Hanning tapered blocks equal to 12 000 points ($T = 60$ s) and average 119 adjacent blocks overlapped by 50%,

[a)]This paper is part of a special issue on COVID-19 Pandemic Acoustic Effects.
[b)]Electronic mail: dahl@apl.washington.edu

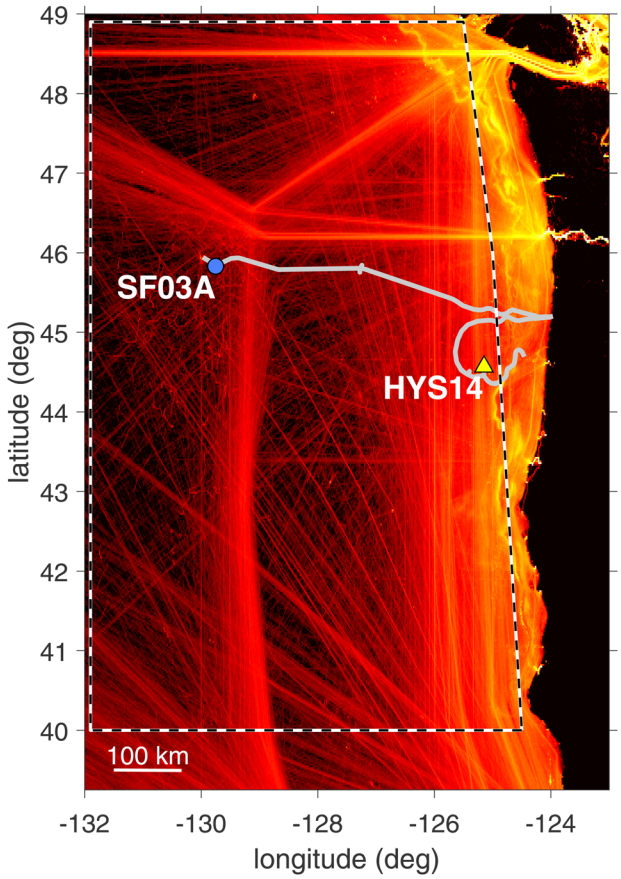

FIG. 1. (Color online) Heat map of AIS reports in the Northeast Pacific Ocean 2015–2020, location of RCA cabling (gray lines), station HYS14 (triangle), and water column measurement site SF03A (circle). The white/black dashed outline identifies the area used to quantify shipping density.

corresponding to a 1-h spectral estimate following Welch's overlapped segment average (e.g., see Percival[5]). These one-sided variance spectra $S_n(f)$ integrate to the mean-square pressure of the corresponding nth-hour non-tapered block. For a given day, the pressure variance spectrum $P_{ms}(f) = \langle S_n(f) \rangle$, in dimension Pa^2/Hz; we also compute $P_{dB}(f)$ equal to $\langle 10 \log_{10} S_n(f) \rangle$, representing a geometric mean over the day. The geometric mean is sensitive to the time scale of the spectral estimate, and after some experimentation, 1 h, as also suggested in Ref. 6, provides the suitable balance that captures longer-term seasonal trends and mitigates the influence of transient events.

Two correlates to the acoustic data are based on direct measurements of the sound speed profile and shipping density. Sound speed is derived from measurements at RCA station SF03A, located 388 km from the HYS14 site (Fig. 1); here a winched shallow-water profiler continuously measures conductivity and temperature over the upper 200 m.

Shipping density is assessed by automatic identification system (AIS) reports[7] distilled into a count of the number of ships with unique International Maritime Organization (IMO) numbers, limited in this study to ships >100 m length within ~600 km west, north, or south of HYS14 (within the white/black dashed line in Fig. 1).

III. RESULTS

A summary of the entire HYS14 hydrophone data set to date is displayed in the stacked image of the daily $P_{dB}(f)$ spanning the period 15 January 2015–17 August 2020 [Fig. 2(a)]. Occasional data interruptions amount to 83 missing days during this period of 5 years and 7 months. Black, dashed rectangles identify known research vessel activity occurring above the sensor (2018) and a nearby seismic survey (2019), which are removed from subsequent analysis.

A prominent seasonal feature of the data is seen in the band centered near 20 Hz, which is consistent with that produced by fin whales (*Balaenoptera physalus*).[8,9] Examining select periods (typically hours in duration) while this signal is present, a representative coherence time scale τ_e, e.g., as defined in Ref. 10, is ~0.25 s, with center frequency ~20.5 Hz. Less prominent is a higher-frequency counterpart, between 40 and 45 Hz; this has been attributed to feeding calls by fin whales,[11] although generally not as contemporaneous with 20-Hz calls as observed here.

For the 20-Hz signal, it is of interest to take the daily average of $P_{ms}(f)$, integrated over the $1/\tau_e$ or the 4-Hz band, 18.5–22.5 Hz, and apply a 30-day moving (geometric) average using the decibel equivalent. Converting back to mean-square pressure, the results agree with Gaussian fits

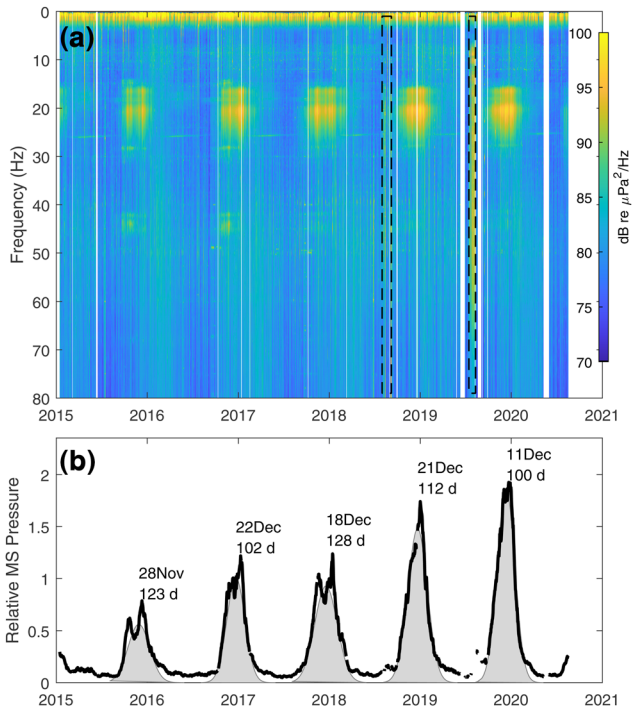

FIG. 2. (Color online) (a) Daily averaged $P_{dB}(f)$ spanning the period 15 January 2015-17 August 2020 for RCA hydrophone HYS14. Black, dashed rectangles identify research vessel activity in 2018 and a seismic survey in 2019. (b) Mean-square pressure as computed from daily averaged $P_{ms}(f)$ integrated over the 18.5–22.5 Hz band and subjected to a 30-day moving geometric average. The mean-square pressures are normalized in the plot such that 1 is mapped to a mean-square pressure equivalent to 100 dB re μPa^2, and 2 is equivalent to 103 dB. A separate Gaussian fit is made for each year (shaded curves) with first moment date and 2σ spread in days annotated.

https://doi.org/10.1121/10.0005192

made for each year to describe behavioral timing, with the date of the first moment falling between 28 November and 22 December and 2σ spread ranging from 100 to 128 days [Fig. 2(b)]. To assess variation, the pre-averaged data are detrended by the moving-average result, yielding an approximately Gaussian variation that is expected[10] with standard deviation ~2.5 dB, most applicable in the vicinity of the period of each first moment date.

The driver of this timing, for example, as in migration or enhanced call activity during breeding periods, is beyond the scope of this study, although it is noteworthy that the mean-square pressure in this band generally increases with advancing year, whereas the 2σ duration in days times mean-square pressure remains approximately constant. We also observe a narrow band tone at ~26 Hz during the minima in fin whale calls, suspected to be a chorus of blue whale (*Balaenoptera musculus*) calls. While individual calls are not discernible in these data, the frequency of the tone modulates with the season and decreases at a rate of 1/8 Hz per year, consistent with other observations in the Southern Hemisphere.[12,13]

These are rich and stand-alone investigations that are important to mention here for context. Our main focus in this study, however, is on noise from shipping, for which we limit our analysis to the third-octave (decidecadal) band spanning 56.23–70.79 Hz centered at 63.10 Hz to be sufficiently separated in frequency from this biophony. This corresponds, for example, to one of the important third-octave bands studied for long-term trends from shipping noise along the U.S. West Coast between 1996 and 2007.[4]

The daily $P_{dB}(f)$ is further averaged over this band, as this is the most effective method to characterize the seasonal pattern in the band spectral level that is linked to annual ocean surface temperature cycles, as reported by others.[14] The geometric average, similar to taking the median, tends to stabilize the variance and reduces the influence of

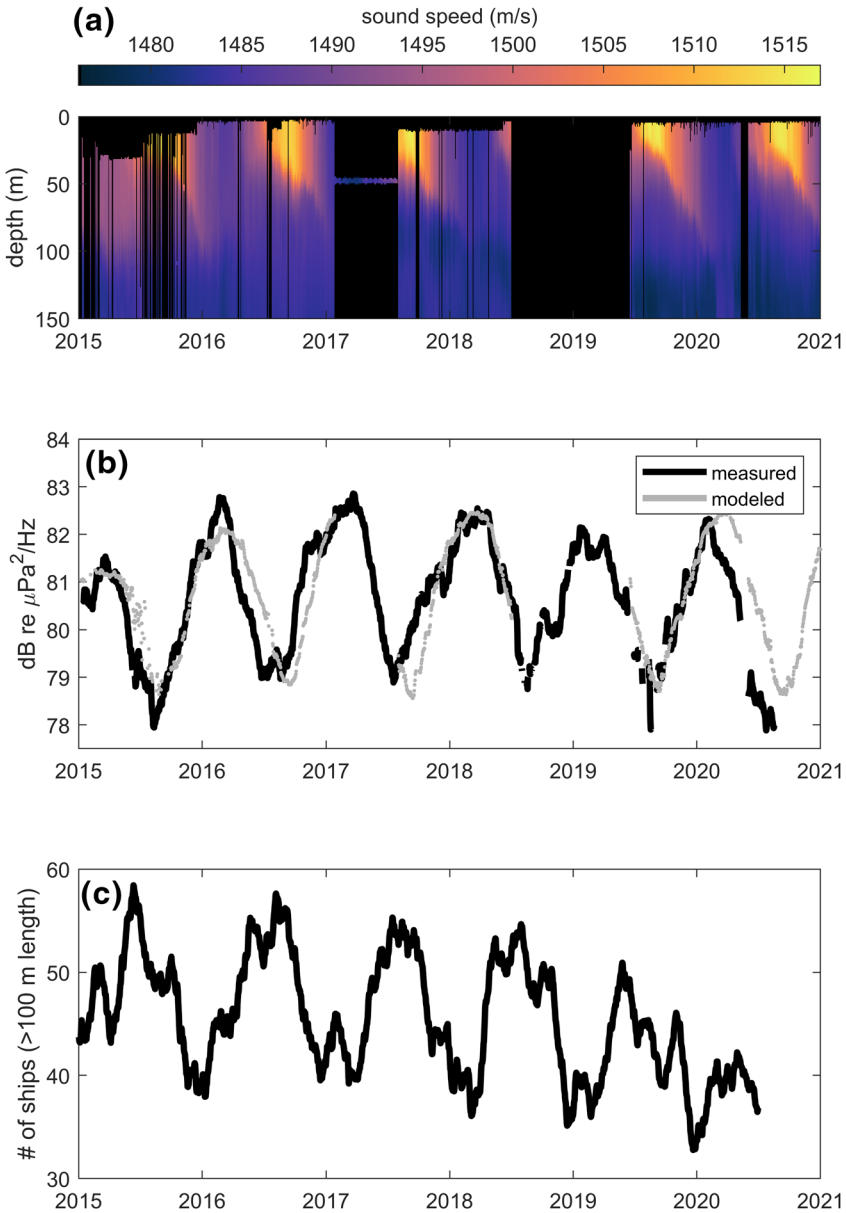

FIG. 3. (Color online) (a) Sound speed profiles measured at SF03A; black regions indicate no data. (b) Average $P_{dB}(f)$ within the 63-Hz third-octave band (black line) smoothed by a 45-day moving average and modeled levels (gray line) based on the measured sound speed profile. (c) A 45-day moving average of number of ships with length >100 m passing within the region indicated in Fig. 1, as identifed by unique IMO number.

episodic high outlying values. Unlike the median, all values contribute to the average.

With seasonal warming and onset of higher ocean surface temperatures, it is expected that mode excitation support moves deeper and thus away from typical ship source depths. Evidence for this comes from converting the shallow-water profiler data from RCA station SF03A to sound speed [Fig. 3(a)], which can be used in simple modeling. A 45-day moving average of $P_{dB}(f)$ (intentionally longer than in the case of the fin whale data) is taken [black line, Fig. 3(b)], which shows a remarkable seasonal trend, and detrending yields a Gaussian variation with standard deviation ∼2 dB. This trend is reasonably captured upon using the sound speed data [Fig. 3(a)][15] and computing an incoherent sum of modes based on mode excitation coefficients for a 60-Hz source at a notional source depth of 5 m multiplied by the respective propagation decay (imaginary part of wavenumber). The results are summed for a uniform distribution of sources from 1 to 600 km, yielding a model (not calibrated) of the seasonal pattern in band spectral level with variation [gray line in Fig. 3(b)] that is in phase with the long-term observations of shipping noise. Wind-related noise will have some influence, but less at frequencies lower than about 100 Hz.[16] However, it is also not plausible for it to be manifested in such a repetitive manner over the course of six annual cycles; furthermore, wind speeds at this site are relatively constant during the year.

Referring to this now as a seasonal propagation effect for near-surface generated shipping noise, it is also evident that ship density as reflected by the daily count of vessels over 100-m length within the box in Fig. 1, is *out of phase* with the seasonal propagation effect, i.e., highest shipping activity generally occurs in mid-year [Fig. 3(c)].

These results (Fig. 3) suggest that any underlying trend in the underwater noise data associated with COVID-19 will necessarily be subtle. To examine this trend, we return to the daily (linear) $P_{ms}(f)$, taking the average over the 63-Hz third-octave band. Operating with daily $P_{ms}(f)$, as with the fin whale case (but here maintaining units of spectral density), is more appropriate given our goal to assess the addition of incoherent sources[17] rather than a seasonal long-term propagation trend (Fig. 3), which uses $P_{dB}(f)$.

The 45-day moving geometric average of the 63-Hz band level is plotted with respect to Julian day for each year (Fig. 4). The seasonal dependence [Fig. 3(b)] is evident, although reduced when based on $P_{ms}(f)$ with a peak-to-trough difference of about 2–3 dB, with the 63-Hz band levels over the six years reaching an annual minimum near day 210.

It is also apparent that the level for year 2020 departs from the previous five years starting at around day 60. The departure is not large but is persistent, starting at about ∼1 dB and increasing to ∼2 dB. This result is notionally consistent with recent results obtained from the Canadian network north of our study site.[18] Grouping the data from the prior five years and computing the mean and standard deviation over time, the gray shaded areas denote $\pm 1\sigma$ and 2σ about this mean trend; after about day 60, year 2020 remains less than this mean trend by at least 2σ.

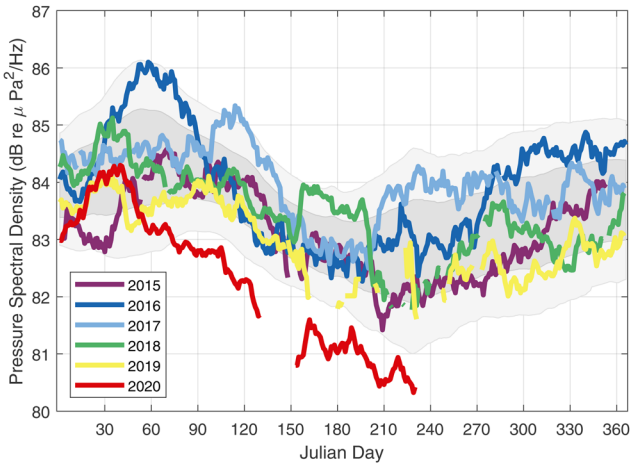

FIG. 4. (Color online) A 45-day moving geometric average of the 63-Hz third-octave band levels for years 2015–2020 (system offline between days 120 and 150 in 2020). Gray shaded areas denote $\pm 1\sigma$ and 2σ about this mean trend based on grouping the data over the first five years and computing the mean and standard deviation over time.

IV. DISCUSSION

The duration over which to compare the influence of suppressed economic activity due to the COVID-19 pandemic on underwater noise levels with prior years is admittedly brief, but the second economic quarter (Q2) of each year provides some corroborating evidence. The Q2 quarterly averages (Table I) of the 63-Hz band levels (Fig. 4) put Q2 of 2020 about 1.6 dB less than the mean of Q2 for the prior five years. Similarly, the 2020 average daily large-vessel count for Q2 (Table I) is reduced by ∼19% upon comparing with the mean of Q2 for the prior five years. It is plausible to assume that noise goes as $10\log_{10}$ of the large-vessel count, with the ∼19% reduction yielding a change of about ∼1 dB, which is nominally consistent. Furthermore, the 2020 Q2 TEU totals for Puget Sound are reduced by ∼17%. It has been proposed[19] that low-frequency shipping noise levels scale with gross tonnage, and possibly this may be a better predictor.

TABLE I. Metrics for Q2 (April–June).

Year	63-Hz band dB re 1 μPa^2/Hz	Quarterly TEU[a]	Traffic (number of vessels)[b]
2015	83.5	925 735	51
2016	83.3	895 732	52
2017	84.1	929 716	47
2018	83.7	940 241	49
2019	83.1	982 961	47
2020	81.9	775 382	40

[a]Twenty-foot equivalent unit (TEU).
[b]Average daily count of vessels length >100 m, passing within the area indicated in Fig. 1.

Note that the estimated reduction of 1.6 dB is less than, for example, the relative reduction in noise levels observed in the rerouting of shipping lanes away from the measurement site, as discussed in the context of the 2008 economic downturn,[20] although it does not appear that rerouting is in effect in our study. Nevertheless, our findings over this shorter period of economic change should be viewed as more substantive in quantifying the reduction in noise level and less so in unraveling the precise causative association with measures of shipping activity.

V. SUMMARY

Underwater noise data measured 87 km off Newport, OR between 15 January 2015 and 17 August 2020 are examined by comparing the 2020 data with that from the prior five years. We find a 1.6-dB reduction in the 63-Hz third-octave band spectral level that is typically associated with underwater noise from shipping. The reduction begins on approximately Julian day 60 of 2020 and is relative to the same period in the prior five years, which we infer is the result of reduced shipping and economic activity impacted by the COVID-19 pandemic. Corroboration of this COVID-19 effect is offered through an analysis of AIS shipping data and shipping container activity for Puget Sound. Our results are subtle and must be understood in the context of the significant seasonality within this band on the order of 4 dB, which is in phase with seasonal changes in Northeast Pacific Ocean temperature in the upper 200 m. The seasonally dependent minimum in noise level is concurrent with the reduced shipping activity during the COVID-19 pandemic.

ACKNOWLEDGMENTS

The acoustic and oceanographic data are based upon work supported by the National Science Foundation under Cooperative Agreement No. 1743430 (which supports the OOI). This research was supported by the University of Washington Cooperative Institute for Climate, Ocean, and Ecosystem Studies with additional support provided by the Office of Naval Research. The Northwest Seaport Alliance is gratefully acknowledged for providing the TEU and other contextual data relating to Puget Sound shipping. P.H.D. also thanks Dr. Rex Andrew of the Applied Physics Laboratory, University of Washington, for the many helpful discussions during the summer of 2020.

[1]D. S. Kelley, J. R. Delaney and Cabled Array Team, "NSF's Cabled Array: A wired tectonic plate and overlying ocean," in *Proceedings of OCEANS 2016 MTS/IEEE Monterey*, Monterey, CA (September 19–23, 2016), pp. 1–10.
[2]Ocean Observatories Initiative, "Regional Cabled Array," https://ocean-observatories.org/regional-cabled-array (Last viewed 2021-03-15).
[3]D. H. Cato, "Shipping noise impacts on marine life," in *Proceedings of Internoise 2014*, Melbourne, Australia (November 16–19, 2014), pp. 1–6.
[4]R. K. Andrew, B. M. Howe, and J. A. Mercer, "Long-time trends in ship traffic noise for four sites off the North American West Coast," J. Acoust. Soc. Am. **129**, 642–651 (2011).
[5]D. P. Percival, "Spectral analysis of univariate and bivariate time series," in *Statistical Methods for Physical Science*, eidted by J. L. Stanford and S. B. Vardeman (Academic Press, San Diego, 1994), pp. 313–348.
[6]S. M. Nichols and D. L. Bradley, "Global examination of the wind-dependence of very low frequency underwater ambient noise," J. Acoust. Soc. Am. **139**, 1110–1123 (2016).
[7]NOAA, "Vessel traffic data," https://marinecadastre.gov/ais/ (Last viewed 2021-03-15).
[8]W. A. Watkins, P. Tyack, K. E. Moore, and J. E. Bird, "The 20-Hz signals of finback whales (*Balaenoptera physalus*)," J. Acoust. Soc. Am. **82**, 1901–1912 (1987).
[9]M. J. Weirathmueller, K. M. Stafford, W. Wilcock, R. S. Hilmo, R. P. Dziak, and A. M. Trehu, "Spatial and temporal trends in fin whale vocalizations recorded in the NE Pacific Ocean between 2003–2013," PLoS One **12**(10), e0186127 (2017).
[10]N. C. Makris, "The effect of saturated transmission scintillation on ocean acoustic intensity measurements," J. Acoust. Soc. Am. **100**, 769–783 (1996).
[11]A. Širović, L. N. Williams, S. M. Kerosky, S. M. Wiggins, and J. A. Hildebrand, "Temporal separation of two fin whale call types across the eastern North Pacific," Mar. Biol. **160**, 47–57 (2013).
[12]E. C. Leroy, J.-Y. Royer, J. Bonnel, and F. Samaran, "Long-term and seasonal changes of large whale call frequency in the southern Indian Ocean," J. Geophys. Res. **123**, 8568–8580, https://doi.org/10.1029/2018JC014352 (2018).
[13]A. N. Gavrilov, R. D. McCauley, and J. Gedamke, "Steady inter and intra-annual decrease in the vocalization frequency of Antarctic blue whales," J. Acoust. Soc. Am. **131**, 4476–4480 (2012).
[14]M. F. McKenna, S. M. Wiggins, and J. A. Hildebrand, "Relationship between container ship underwater noise levels and ship design, operational and oceanographic conditions," Sci. Rep. **3**, 1760 (2013).
[15]Modes computed by appending the SF03A sound speed data (0–200 m) to full-depth sound speed profiles from the RCA deep profiler at nearby station DP03A (200–2640 m) and assuming a sediment halfspace defined by speed 1600 m/s, attenuation 0.1 dB/λ, and density 1600 kg/m^3.
[16]R. K. Andrew, B. M. Howe, J. A. Mercer, and M. A. Dzieciuch, "Ocean ambient sound: Comparing the 1960s with the 1990s for a receiver off the California coast," Acoust. Res. Lett. Online **3**, 65–70 (2002).
[17]N. D. Merchant, P. B. Blondel, D. T. Dakin, and J. Dorocicz, "Averaging underwater noise levels for environmental assessment of shipping," J. Acoust. Soc. Am. **132**, EL343–EL349 (2012).
[18]D. J. Thomson and D. R. Barclay, "Real-time observations of the impact of COVID-19 on underwater noise," J. Acoust. Soc. Am. **147**, 3390–3396 (2020).
[19]G. V. Frisk, "Noiseonomics: The relationship between ambient noise levels in the sea and global economic trends," Sci. Rep. **2**, 437 (2012).
[20]M. McKenna, S. Katz, S. Wiggins, D. Ross, and J. Hildebrand, "A quieting ocean: Unintended consequence of a fluctuating economy," J. Acoust. Soc. Am. **132**, EL169–EL175 (2012).

Vector Acoustic Analysis of Time-Separated Modal Arrivals From Explosive Sound Sources During the 2017 Seabed Characterization Experiment

Peter H. Dahl, *Senior Member, IEEE*, and David R. Dall'Osto

***Abstract*—The Intensity Vector Autonomous Recorder (IVAR) is a system that records four coherent channels of acoustic data continuously: one channel for acoustic pressure and three channels associated with a triaxial accelerometer from which acoustic particle velocity is obtained. IVAR recorded the vector acoustic field in broadband signals originating from Signal, Underwater Sound (SUS) (Mk-64) charges deployed at 5–13-km range from the fixed IVAR site (mean depth 74.4 m) as part of the 2017 Seabed Characterization Experiment (SBCEX) designed to study the acoustics of fine-grained muddy sediments. Sufficient geometric dispersion at these ranges permitted unambiguous identification of up to four modes as a function of frequency for frequencies less than 80 Hz. From time–frequency analysis of the dispersed arrivals, a single mode (n) and single-frequency (f_i) properties are identified at peaks in the narrowband scalar field, with time dependence corresponding to mode group speed. At these time–frequency addresses, four quantities derived from the vector acoustic measurements are formed by coherent combination of pressure and velocity channels: first, modal phase speed; second, circularity, a measure of the normalized curl of active intensity; third, depth-dependent mode speed of energy; and fourth, vertical component of reactive intensity normalized by scalar intensity. A means to compute these quantities theoretically is provided, and a comparison of model results based on a notional geoacoustic representation for the SBCEX experimental area consisting of a single low-speed mud layer over a half-space area versus a Pekeris representation based on the same half-space shows a striking difference, with the field observations also clearly at variance with the Pekeris representation. A fundamental property of mode 2, observed at the IVAR location, is a change in sign for circularity and vertical reactive intensity near 37 Hz that is posited as a constraint observation for mode 2 that must be exhibited by any geoacoustic model that includes a low-speed mudlike layer applied to this location.**

***Index Terms*—Acoustic particle velocity, active intensity, circularity, group speed, modal speed of energy, phase speed, reactive intensity, vector acoustics.**

Manuscript received September 14, 2018; revised January 8, 2019; accepted February 26, 2019. This work was supported by the U.S. Office of Naval Research, Code 32, Ocean Acoustics Program, under ONR Grant N00014-16-1-2484 and Grant N00014-16-1-2571 (development of the Intensity Vector Autonomous Recorder). *(Corresponding author: Peter H. Dahl.)*

Guest Editor: P. Wilson.

P. H. Dahl is with the Applied Physics Laboratory and the Department of Mechanical Engineering, University of Washington, Seattle, WA 98105 USA (e-mail: dahl@apl.washington.edu).

D. R. Dall'Osto is with the Applied Physics Laboratory, University of Washington, Seattle, WA 98105 USA (e-mail: dallosto@apl.washington.edu).

Digital Object Identifier 10.1109/JOE.2019.2902500

I. Introduction

THE Intensity Vector Autonomous Recorder (IVAR) is a system that records four coherent channels of acoustic data continuously: one channel for acoustic pressure and three channels associated with a triaxial accelerometer from which acoustic particle velocity is obtained. IVAR was deployed on the seafloor during the Seabed Characterization Experiment (SBCEX), conducted 95 km south of Martha's Vineyard, MA, USA, in 2017. The primary goal of the SBCEX is to study the acoustics of fine-grained muddy sediments that are a prominent feature of the experimental area. For example, the upper most sediment layer commencing at the water–sediment interface is known to consist of fine-grained mudlike material [1] with geoacoustic properties largely unknown before the SBCEX [2].

The IVAR was deployed on the seafloor from *R/V Endeavor* during the SBCEX for two periods: 7 March 1645Z to 9 March 1415Z (45.5 h) and 17 March 2330Z to 18 March 2030Z (22 h). During both deployments, the IVAR recorded signals (frequency range 50–500 Hz) from a towed source (J-15) deployed from *R/V Endeavor*, the noise field from large cargo vessels operating nearby, and signals from the various experimental sound sources used by other investigators during the SBCEX.

During the second deployment, the IVAR recorded arrivals from broadband SUS (Mk-64) charges deployed from *R/V Neil Armstrong*. The focus of this study is on the IVAR observations of SUS deployments at ranges 5–13 km from the fixed IVAR location. At these ranges and in view of the ∼74-m depth, there is sufficient geometric dispersion of the broadband explosive SUS pulse to allow identification of four distinct modes below 80 Hz.

This work does not engage in a geoacoustic inversion of field results *per se*; instead it presents a purely observational description of four quantities derived from the vector acoustic measurements that are sensitive to modal properties as realized at the IVAR site. These quantities are formed by the coherent combination of pressure and particle velocity and are as follows:

1) modal phase speed;
2) circularity, a measure of the normalized curl of active intensity;
3) depth-dependent mode speed of energy;
4) the vertical component of reactive intensity normalized by scalar intensity.

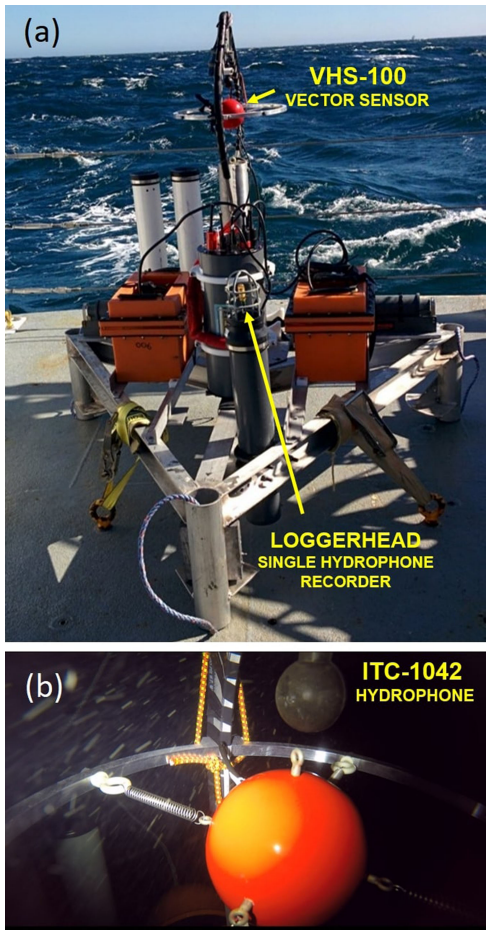

Fig. 1. Annotated photographs of IVAR (a) on aft deck of *R/V Endeavor* and (b) as deployed on seafloor. Streaks are marine snow carried by the ocean current.

To guide interpretation and provide a pathway to exploit these properties in geoacoustic inversion, a method to compute these quantities theoretically using a normal mode-based propagation code is also provided, and we present computed forms associated with a notional geoacoustic model. For example, we will demonstrate an important property of mode 2 as it goes through a transition in the neighborhood of 37 Hz; the existence of this transition and its location in frequency appears to be strongly dependent on the surficial low-speed mud layer at the IVAR site.

This paper is arranged as follows: in Section II, the IVAR system is described with key details relating to its second deployment and measurement of SUS charges. Section III describes the data processing, first covering broadband vector intensity for context, and then addressing the narrowband processing more closely associated with this study. In Section IV, the vector acoustic quantities for single-mode single frequency are formally defined along with corresponding models, and field results are presented in Section V. A summary and some additional remarks are provided in Section VI.

II. IVAR System and Deployment During SBCEX

The IVAR system consists of a bottom-deployed tripod [see Fig. 1(a)] where key components include a three-axis accelerometer contained within a 10-cm diameter neutrally buoyant sphere (VHS-100, Ocean Applied Acoustics) and an omnidirectional hydrophone (ITC-1042) positioned 10 cm above the center of the sphere. The accelerometer and hydrophone are coherently recorded (25 000-Hz sample rate), in four low-gain (0 dB) and four high-gain (30 dB) channels. Key metadata including water depth and sensor orientation were recorded every 15 s over the duration of the deployment. Because it was important to verify proper suspension of the neutrally buoyant sphere, a video record was taken for each deployment to document the descent phase of IVAR and first few minutes on the seafloor [see Fig. 1(b)]. Note that a second single-hydrophone recording system (Loggerhead Instruments, Inc., Sarasota, FL, USA) is also mounted on the IVAR to provide a back-up set of hydrophone data although this data stream is not recorded coherently with accelerometer data.[1]

Combining co-located and coherently measured particle velocity with pressure provides a direct measure of vector intensity. Particle velocity as measured over three axes is obtained, depending on processing application, by either time integration or frequency division of the acceleration channels. With radius $a = 5$ cm and k equal to acoustic wave number based on sound speed in water, the neutrally buoyant sphere responds sufficiently similar to an accelerating parcel of water for frequencies up to about $ka \sim 0.8$, or 3750 Hz [3], although we limit our study to frequencies less than 1000 Hz to avoid any need for vertical phase corrections between pressure and particle velocity. Measurements at higher frequencies are still possible but ultimately the integrated pressure distribution over the surface of the sphere divided by mass of water displaced will not equate to acoustic particle acceleration for an equivalent volume of water.

At low frequencies, all channels are limited by the highpass filtering (-3 dB corner frequency equal to 25 Hz).[2] Owing to the roll-off in particle acceleration with frequency, reliable particle velocity estimates at 25 Hz require signal levels greater than about 120 dB re 1 μ Pa, whereas the pressure channel could detect somewhat lower levels.

For the second deployment, the IVAR was placed at location 49.48655 °N, -70.63831 °W where mean water depth was 74.4 m varying by ± 0.4 m owing to the M2 tidal variation [see Fig. 2(a)]. A CTD cast taken from *R/V Endeavor* [see Fig. 2(b)] shortly before recovery of IVAR shows a relatively well-mixed water column typical of other observations made during SBCEX [4]. In our subsequent manipulation of vector acoustic data, we implement the depth average as representing an isovelocity water column, with sound speed $c_w = 1468.3$ m/s.

The broadband source was the Mk-64 SUS charge consisting of 31 g of tetryl designed to detonate at notional depth of 18.3 m. These sources were deployed from *R/V Neil Armstrong* at locations (SUS stations) planned and coordinated by P. Wilson and D. Knobles and a separate study related to these sources is in preparation. At each station, a sequence of five SUS charges

[1] Some researchers in SBCEX are utilizing this hydrophone data for purposes of geoacoustic inversion.

[2] In hindsight, this was an overly conservative setting meant to protect the channels from possible saturation from very nearby sources. For future studies, we have set a lower corner frequency to 8 Hz.

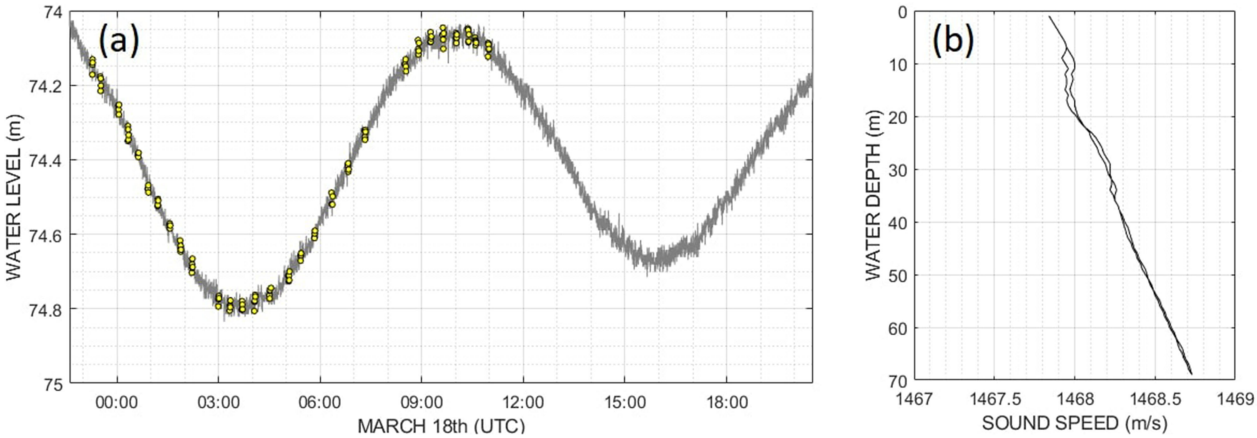

Fig. 2. (a) Water level measured by a depth sensor on the IVAR tripod, time of SUS charges indicated by circles. (b) Sound speed versus depth made by conductivity–temperature–depth (CTD) cast from *R/V Endeavor*; average speed equals 1468.3 m/s.

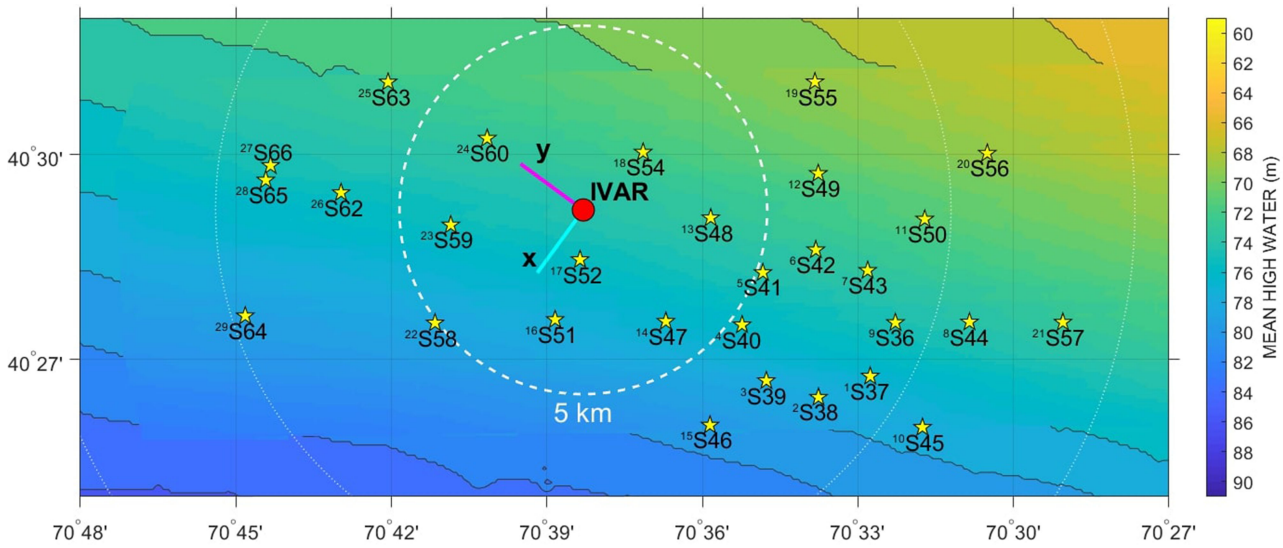

Fig. 3. Distribution of Mk-64 SUS detonation stations (stars) observed by the IVAR system (red circle); orientation of *x*-axis (cyan) and *y*-axis (magenta) indicated. Analysis is based on 22 stations outside the dashed circle delineating range 5 km from the IVAR. Note that each SUS detonation station presents a unique orientation with respect to the *x* and *y* axes of the IVAR system, e.g., the response from station S40 is manifested primarily on the *y*-axis.

were deployed separated in time by approximately 20 s. The second deployment of the IVAR coincided with a subset of SUS deployments, a total of 29 stations for which the range between SUS detonation (*R/V Neil Armstrong*) and IVAR location on the seabed varied between 3 and 13 km (see Fig. 3). However, to realize sufficient geometric dispersion, we limit this analysis to the 22 stations that fall outside the dashed circle in Fig. 3. The center of the neutrally buoyant sphere on the IVAR was positioned 1.25 m above the seafloor, with the *x*-axis aligned with true bearing 216.3° and *y*-axis aligned with 306.3°. For example, the bearings to stations S40 and S45 (see Fig. 3) are aligned with the *y*-axis.

III. Calculating Acoustic Energy Density and Vector Intensity

A. Broadband Vector Intensity

In the following, broadband pressure $P(t)$ and components of particle velocity $V_{x,y,z}(t)$, over the bandwidth 10–1000 Hz, are discussed briefly where the latter are obtained by time integration of the measured acceleration time series (although levels for frequencies less than 25 Hz are reduced somewhat owing to the aforementioned highpass filtering.) Results from a single detonation (see Fig. 4) from SUS station S40, range 5 km, shows the broadband, potential energy density $(1/2)|P(t)|^2/(\rho c_w^2)$ and kinetic energy density $(1/2)\rho|V(t)|^2$, as each varies over time. These are based on water density, ρ equal to 1027.6 kg/m^3, and c_w equal to 1468.3 m/s. The relative time reference is set by the arrival of the peak waterborne path, and a time average over relative time period 0–0.5 s brings the two energy densities to within 0.14 dB (the 0.5-s time averaging period encompassing 99% of the energy.)

The segment of data commencing ∼450 ms before arrival of the peak waterborne path (relative time equal to 0) suggests the onset of a ground wave [5] associated with the emergence of mode 2 at frequency ∼22 Hz. This frequency inferred from the pattern in Fig. 4 made clear in this decibel view, with 22 Hz being too high for the cutoff of mode 1 given the water depth. Note

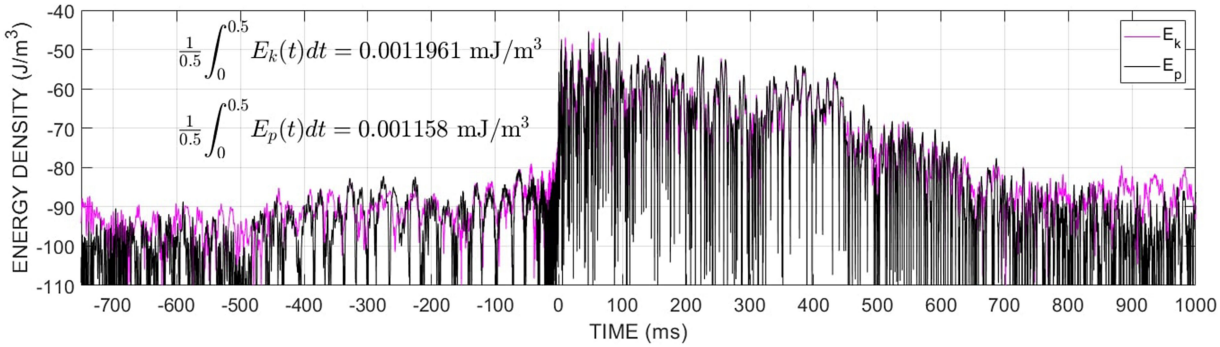

Fig. 4. Time-varying potential (black) and kinetic (magenta) energy densities measured at the IVAR site from a SUS arrival originating at station S40, range 5 km. Time is relative to the arrival of the peak waterborne path.

that the mode 2 precursor is evident in the kinetic energy density but somewhat more poorly resolved by the velocity channels because of the highpass filtering mentioned in Section II. Similarly, the relatively narrowband region (frequency ∼28 Hz) centered about 400 ms after arrival of the peak waterborne path is likely associated with the Airy phase for mode 2; this frequency being more readily inferred from the same pattern upon expanding the scale. The received waveform embodies the expected bubble pulse [6] of period ∼42 ms as can be confirmed with autocorrelation. The bubble pulse can produce the interference that is observed primarily at frequencies greater than about 500 Hz, at frequency intervals ∼24 Hz. However, the bubble pulse effect is not problematic for this analysis and we make no further attempt to remove it.

Shown on a linear scale are corresponding broadband pressure (see Fig. 5, top row) and components of particle velocity (see Fig. 5, middle row), where owing to the alignment of the *y*-axis of the vector sensor with source direction of SUS station S40, the *y*-component dominates over the *x*-component. The Umov vector $S_{x,y,z}(t)$ or instantaneous intensity (see Fig. 5, bottom row) is formed by multiplying $P(t)$ by separate components of particle velocity.

The time average of the components of the broadband Umov vector over the same 0–0.5 s period yields estimates of the active intensity vector, with values for the separate components identified. Note that the value of the *y*-component of active intensity is close to an equivalent time average of $(P(t)^2/\rho c_w)$, or scalar intensity, a result anticipated given that the *y*-component of particle velocity normalized by ρc_w approximately equals the pressure for this case that is the representative of a single active source with dominant energy flux in the horizontal direction. The *z*-component of the broadband Umov vector varies between negative and positive values; this change in direction of the sound field flow is indicative of reactive intensity [7], as defined and discussed in Section III-B. There exists a small nonzero time average in the positive z (downward) direction, and we observe the broadband vertical flux to be in general 0.03–0.04 times the corresponding horizontal flux for the 22 stations (see Fig. 3) studied.

In the remainder of this study, we examine properties associated with both active and reactive intensities in greater detail as function of mode and frequency, made possible by the geometric dispersion of the SUS arrivals for ranges greater than about 5 km. The frequency range studied will necessarily be limited to <80 Hz, where there is sufficient time separation among modes. New notation for complex narrowband pressure and particle velocity is necessary along with model counterparts as a function of mode and frequency. We avoid reusing $P(t)$ and $V_{x,y,z}(t)$, reserving these for real broadband quantities.

B. Time–Frequency Analysis

Time–frequency analysis is done with a bank of bandpass filters applied to the original data in the time domain (using the low-gain set of channels in all cases), each with bandwidth B equal to 4 Hz centered at frequencies between 10 and 80 Hz, every 1 Hz. We use this approach rather than, say, an equivalent one involving short-time Fourier transforms, as our preference is to use intensity units over spectral densities.

An analytic signal is formed from the measured narrowband filtered time series for pressure $p_{M_i}(t)$, centered at f_i, by constructing a Hilbert-transformed pair $p_i(t) = p_{M_i}(t) + i\hat{p}_{M_i}(t)$, where $\hat{p}_{M_i}(t)$ is the Hilbert transform of the signal that is 90° out of phase with $p_{M_i}(t)$. The analytic signal $p_i(t)$ is henceforth used as a complex representation of the pressure data. Potential energy density $E_{p_i}(t)$ (J/m^3) as a function of time and centered at f_i is thus

$$E_{p_i}(t) = \frac{1}{4}|p_i(t)|^2/(\rho c^2). \tag{1}$$

An image of $E_{p_i}(t)$ [see Fig. 6(a)] for one of the five SUS detonations at station S45 (range 10 km) shows the arrival separated into the first four modes. Results from the other four detonations from S45 are similar. We can easily identify the maximum value of $E_{p_i}(t)$ for each mode and frequency, the time–frequency locations for which are identified by the dots in Fig. 6(a). These time–frequency addresses are an important part of our analysis to identify modes as a function of frequency.

Time series for the three components of complex velocity, as in the *x*-component v_{x_i} centered at f_i are calculated by dividing the complex representation of the corresponding measured and narrowband filtered acceleration channel a_{x_i} by $-i2\pi f_i$, where a_{x_i} also represents a Hilbert-transformed pair. The kinetic energy density $E_{k_i}(t)$ is thus

$$E_{k_i}(t) = \frac{1}{4}\rho(|v_{x_i}(t)|^2 + |v_{y_i}(t)|^2 + |v_{z_i}(t)|^2). \tag{2}$$

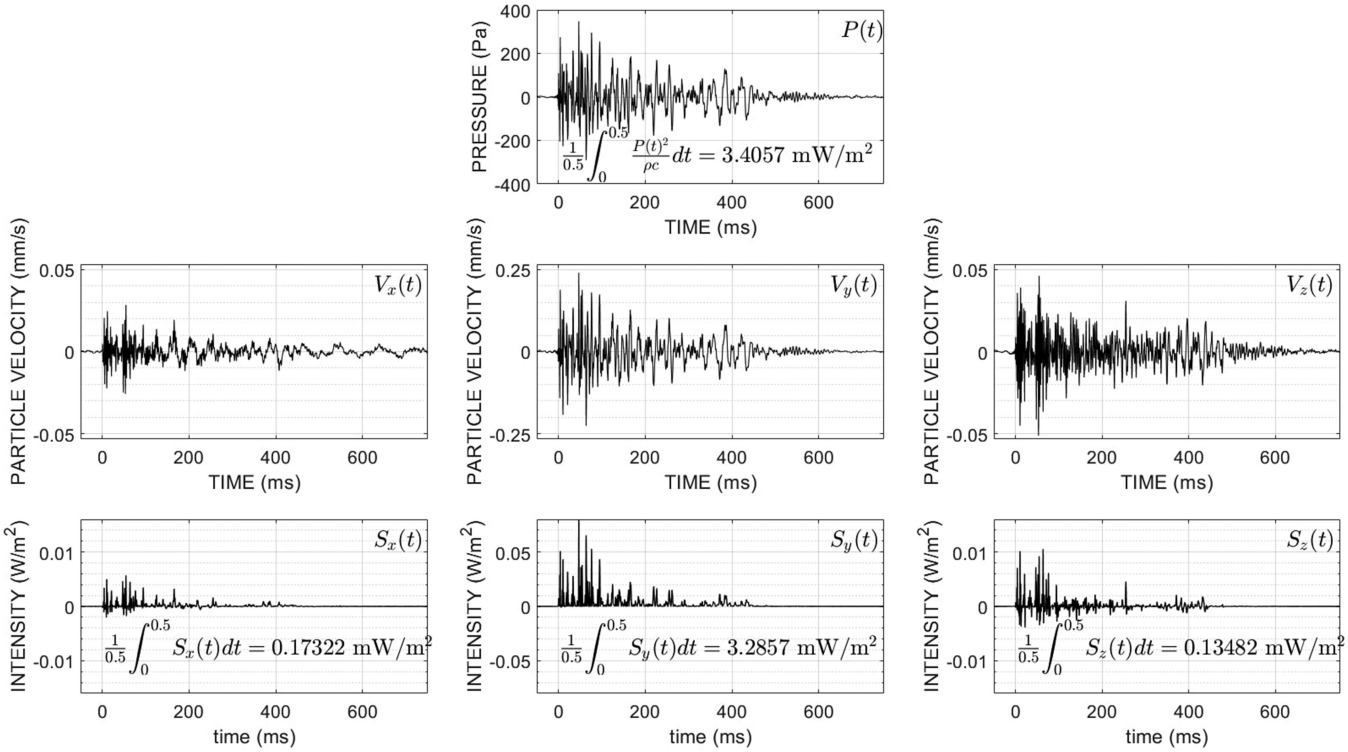

Fig. 5. Top row: Broadband pressure $P(t)$ corresponding to the data in Fig. 4, with time relative to the arrival of the peak waterborne path, also identified is the time average of squared pressure divided by ρc_w . Middle row: Components of broadband particle velocity $V_{x,y,z}(t)$ corresponding to $P(t)$. Note the y-axis for the component V_y ranges from ± 400 Pa when multiplied by ρc_w for ready comparison with $P(t)$. Bottom row: Components of the broadband Umov vector $S_{x,y,z}(t)$ and corresponding time averages.

An image of $E_{k_i}(t)$ [see Fig. 6(b)] closely mirrors $E_{p_i}(t)$, as anticipated from the broadband results (see Fig. 4).

Complex intensity $\vec{I}_c$ as formulated by Heyser [8] is computed as

$$\vec{I}_c = \frac{1}{2} p v^*_{x,y,z} \tag{3}$$

where the asterisk denotes complex conjugate. Taking the real part of $\vec{I}_c$ yields the active intensity, for which the y-component $I_{y_i}(t)$ is shown in Fig. 6(c); taking the imaginary part yields reactive intensity, where the z- or vertical-component $Q_{z_i}(t)$ is shown in Fig. 6(d) and subscript i denotes a central frequency index for these narrowband quantities. Both $I_{y_i}(t)$ and $Q_{z_i}(t)$ also separate into four modes for frequencies less than about 80 Hz. To emphasize these modal patterns, the data are only plotted where the corresponding $E_{p_i}(t)$ is within 12 dB of the maximum.

Looking ahead, we select and study values of second-order quantities including $I_{y_i}(t)$, $Q_{z_i}(t)$, and others to be defined, that are associated with the time–frequency addresses shown by the dots in Fig. 6(a). For example, a narrowband version of the Umov vector $S_y(t)$ in the y-direction at central frequency $f_i = 45$ Hz [see Fig. 6(e)] is formed by

$$S_{y_i}(t) = \mathrm{Re}\{p_i(t)\}\mathrm{Re}\{v_{y_i}(t)\}. \tag{4}$$

Active intensity $I_{y_i}(t)$ corresponding to a cut along 45 Hz [see Fig. 6(c), black line] finds support at modes 1, 2, and 3 [see Fig. 6(e)]. We may interpret $I_{y_i}(t)$ as a slowly varying average value [7], [9] of $S_{y_i}(t)$. More specifically, time integrals of $S_{y_i}(t)$ and $I_{y_i}(t)$ are equal; furthermore, in this narrowband context, $S_{y_i}(t)$ can be approximately reconstructed by multiplying $I_{y_i}(t)$ by $2\cos^2(2\pi f_i t - \phi)$ [10], where ϕ is a phase factor.

Values of $I_{y_i}(t)$ shown by the three black symbols correspond with the time–frequency addresses as extracted from $E_{p_i}(t)$. A similar cut along 30 Hz [see Fig. 6(c), red line] finds support at only modes 1 and 2 given 30 Hz is below the cutoff of mode 3; here, two values of $I_{y_i}(t)$ [see Fig. 6(e), red symbols] correspond with time–frequency addresses.

Vertical reactive intensity $Q_{z_i}(t)$ corresponding to a cut along 45 Hz [see Fig. 6(d), black line] also finds support at modes 1, 2, and 3 [see Fig. 6(f)]. In this case, the vertical component of the Umov vector $S_{z_i}(t)$ time averages to nearly or exactly zero and $Q_{z_i}(t)$ traces the envelope, with $S_{z_i}(t)$ approximately reconstructed by multiplying $Q_{z_i}(t)$ by $\sin(4\pi f_i t - \phi)$ [10]. We observe that for 45 Hz, the envelope $Q_{z_i}(t)$ at the selected values identified by black symbols is negative for modes 1 and 2 and then goes positive for mode 3. (Note: it is the *change* in sign of $Q_{z_i}(t)$ that is important, without physical significance placed on sign [11] other than it be consistent with our time convention of $e^{-i\omega t}$.) A cut along 30 Hz [see Fig. 6(d), red line] finds support at only modes 1 and 2, with the envelope $Q_{z_i}(t)$ shown in Fig. 6(f) along with two selected values identified by the red symbols. In this case, envelope $Q_{z_i}(t)$ for mode 2 is positive. The change in the sign of $Q_{z_i}(t)$ for mode 2 near $\sim$37 Hz is a significant feature of the modal structure as measured at the IVAR location.

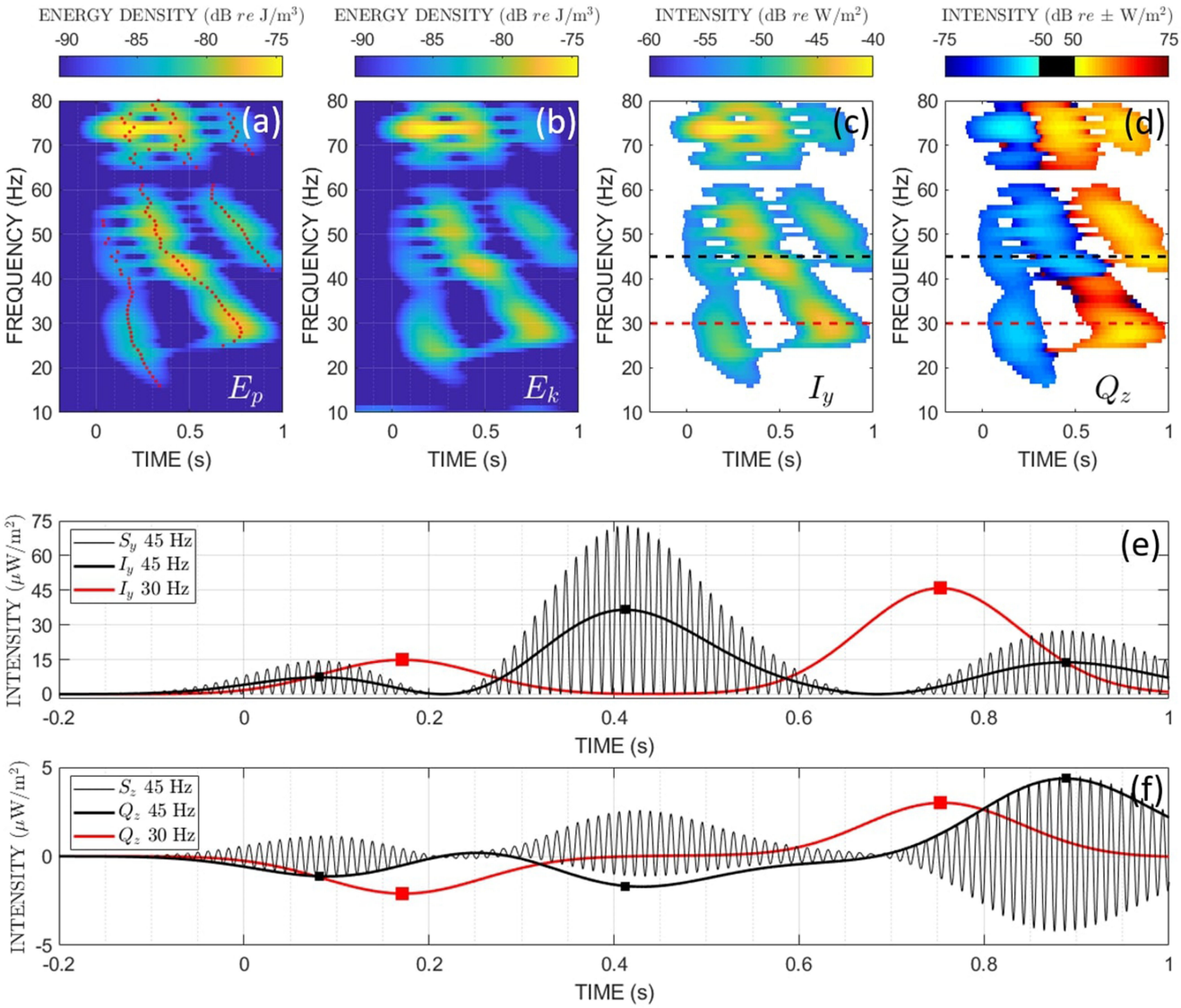

Fig. 6. (a) $E_{p_i}(t)$ measured for one of the five SUS detonations from station S45 (range 10 km). Dots corresponding to maximum values of $E_{p_i}(t)$ identify time–frequency addresses for each mode. (b) Corresponding $E_{k_i}(t)$. (c) and (d) Corresponding $I_{y_i}(t)$ and $Q_{z_i}(t)$ for which thresholding is applied; dashed horizontal lines denote cuts at central frequencies 30 and 45 Hz. (e) Cuts of $I_{y_i}(t)$ along central frequencies 30 Hz (red) and 45 Hz (black) with $S_{y_i}(t)$ centered at 45 Hz also shown for reference. Red and black symbols identify values selected from $I_{y_i}(t)$ to be used in subsequent calculations. (f) Cuts of $Q_{z_i}(t)$ along central frequencies 30 Hz (red) and 45 Hz (black) with $S_{z_i}(t)$ centered at 45 Hz also shown for reference. Red and black symbols identify values selected from $Q_{z_i}(t)$ to be used in subsequent calculations.

IV. Four Quantities Derived From Vector Acoustic Measurements for Single-Mode Single-Frequency and Corresponding Models

The intensity and energy quantities at the individual mode arrivals obtained from the approach outlined in Section III can be combined into four range-independent quantities: phase speed, depth-dependent modal speed of energy, circularity, and normalized vertical reactive intensity. These quantities are sensitive to the geoacoustic properties at the sensor location, and field data from IVAR yield estimates for modes 1–4 and frequencies between about 15 and 80 Hz (with some gaps due to multimode interference near cutoff frequencies). For each quantity, we describe means to obtain a theoretical model developed from a vertical mode function and corresponding horizontal wave number $k_n(f)$. Any normal mode-based propagation code can be used to obtain these quantities; in our case, we use the Kraken [12] normal mode program (with quantities conjugated as necessary to align with our time convention of $e^{-i\omega t}$).

A. Phase Speed $v_{p_n(f)}$

The phase speed for mode n at frequency f is $v_{p_n(f)}$ and we adapt (27) from Mann *et al.* [10] to estimate $v_{p_n(f)}$ at discrete frequencies f_i from the data as follows:

$$v_{p_n(f_i)} = \frac{2c_w^2 E_{p_i}(t_n)}{|I|}. \tag{5}$$

Here, $E_{p_i}(t_n)$ denotes a value selected from $E_{p_i}(t)$ at the time–frequency address [see Fig. 6(a)] corresponding with mode n and frequency f_i, and similarly $|I| =$

$\sqrt{I_{x_i}^2(t_n) + I_{y_i}^2(t_n) + I_{z_i}^2(t_n)}$. For example, Fig. 6(e) (red symbols) identifies the selected values of $I_{y_i}(t_n)$ for the first two modes $n = 1, 2$ at $f_i = 30$ Hz. We adapt this notation for other metrics to be defined subsequently as in the corresponding values of $Q_{z_i}(t_n)$ [see Fig. 6(f)].

A model for phase speed is always available from a normal mode-based propagation code. Note the modal phase speed remains a local quantity, relating to the conditions that gave rise to the local mode properties, as distinct from the modal group speed that is a range-integrated quantity [13].

B. Depth-Dependent Mode Speed of Energy $u_{e_n}(z, f)$

D'Spain *et al.* [14] define a velocity of acoustic energy density transport as the ratio of active horizontal intensity to total energy, each expressed as a function of frequency, with the interpretation of this spectral ratio being the speed of net transport of acoustic energy density at the point in space where the measurement is made. The ratio is bounded by the sound speed in the medium c_w. For example, D'Spain *et al.* [14] show that the speed of energy associated with a diffuse background sound field is only about 10%–50% of the medium's sound speed, whereas this speed, when associated with more spatially concentrated sound sources, approaches c_w. This property thus relates to the relative balance between active (concentrated) and reactive (diffuse) fields, with a completely active field reaching a speed c_w and reactive field having a speed equal to 0 [15].

The variable $u_{e_n}(z, f)$ is closely analogous to this definition with the distinction that $u_{e_n}(z, f)$ is designated for individual modes n, and the point in space need only be a function of measurement depth z_m, i.e., the value of $u_{e_n}(z, f)$ does not depend on measurement range. We estimate depth-dependent mode speed of energy from the data using

$$u_{e_n}(z_m, f_i) = \frac{|I_r|}{E_{p_i}(t_n) + E_{k_i}(t_n)} \tag{6}$$

where $|I_r|$ is the magnitude of active intensity in the horizontal direction and equal to $\sqrt{I_{x_i}^2(t_n) + I_{y_i}^2(t_n)}$.

A model for $u_{e_n}(z, f)$ follows from a few variables generated by a mode-based propagation code using local geoacoustic properties and water depth at the measurement site. We start by representing the complex pressure P_n associated with the nth normal mode at range R and receiver depth z as

$$P_n = \frac{e^{ik_n R - i\frac{\pi}{4}}}{\sqrt{k_n R}} U_n(z_s, f) U_n(z, f) \tag{7}$$

where $U_n(z, f)$ is a vertical mode function, z_s is the source depth, and an asymptotic representation for the Hankel function $H_0(k_n R)$ is used. Note that everything to the left of $U_n(z, f)$ in (7) can be represented by a complex constant, call it A_n. Continuing with the single-mode single-frequency representation, the corresponding horizontal particle velocity V_{r_n} is

$$V_{r_n} = A_n k_n U_n(z, f)/(2\pi f \rho) \tag{8}$$

where a second term in V_{r_n} associated with the horizontal derivative becomes negligible compared with the first term for ranges greater than a few wavelengths and is thus ignored here. The corresponding vertical particle velocity V_{z_n} is

$$V_{z_n} = A_n i \frac{dU_n(z, f)}{dz}/(2\pi f \rho). \tag{9}$$

Henceforth, let the abbreviations P_n, V_{r_n}, and V_{z_n} stand for complex pressure, horizontal velocity, and vertical particle velocity, respectively, for mode n, with each being a function of depth and frequency.

The model for depth-dependent mode speed of energy is thus

$$u_{e_n}(z, f) = \frac{\mathrm{Re}\{P_n V_{r_n}^*\}}{0.5|P_n|^2/(\rho c_w^2) + 0.5\rho(|V_{r_n}|^2 + |V_{z_n}|^2)} \tag{10}$$

where the numerator is represented by single-mode depth-dependent horizontal flux and the denominator is composed of single-mode depth-dependent potential and kinetic energy densities.[3]

We remark that the single-mode vertical flux $\mathrm{Re}\{P_n V_{z_n}^*\}$ equals 0, though for simultaneous arrivals of two or more modes at the same frequency, there can be nonzero vertical flux. This interesting effect is under study but is beyond the scope of this paper. Furthermore, in evaluating the model associated with a single mode, the factor A_n is common to both the numerator and denominator and thus cancels. Therefore, the range R along with cylindrical spreading does not enter into the model result. The three models to be defined below also share this property.

It is tempting to interpret $u_{e_n}(z, f)$ as a modal group speed. However, if we evaluate the quantities in (10) for all depths and take the depth integrals of the numerator and denominator separately, we arrive precisely at the group speed for mode n and frequency f as shown by Tolstoy [16]. In that work, $2E_k$ is used instead of $E_p + E_k$, which is a statement of Rayleigh's principle [17], where integrals over the depth of the kinetic and potential energy densities are equal. Nonetheless, given our measurements are at a single depth, we show that $u_{e_n}(z, f)$ differs greatly from a modal group speed even though it displays a high degree of sensitivity to changes in geoacoustic parameters.

C. Circularity $\theta_n(z, f)$

The phase and amplitude difference in orthogonal components of the particle velocity determines the trajectory of particle motion. For example, if at some position in the field, narrowband horizontal and vertical particle velocities are of equal amplitude and 90° out of phase, the result is a perfectly circular trajectory. The other extreme is when particle velocity exists as a single component, as in single plane wave, producing a trajectory along a line. In between these two extremes, the trajectory can be elliptical [18].

The trajectory pattern is described by the variable circularity θ, which ranges from ± 1 (circular, with sign defining rotational direction) to 0 (trajectory along a line). In general, circularity is a vector with x, y, and z components describing the trajectory of particle motion projected onto the $y - z$, $x - z$, and

[3]Factors of 1/2 in (1) and (2) are absent here as these manipulations do not involve a Hilbert transform.

$x-y$ planes, respectively, computed using the normalized vector product of complex-valued particle velocity $\vec{v}$ [19], as in

$$\vec{\theta} = \frac{\mathrm{Im}\{\vec{v} \times \vec{v^*}\}}{|\vec{v}|}. \tag{11}$$

Circularity may also be interpreted as the normalized curl of active intensity [20].

For many geometries describing an underwater waveguide, it is both practical and realistic to discuss circularity as a scalar metric with horizontal and vertical particle velocities establishing particle trajectory in the range–depth $(r-z)$ plane. For example, such a trajectory is readily observed with a vector sensor lowered through an acoustic field simulating a Lloyd's mirror condition [22]. Measurements of scalar circularity θ as it evolves with a varying source depth that produced a change in multipath interference structure have also been used in geoacoustic inversion [19].

In this paper, we use scalar circularity defined as a function of mode number, measurement depth, and frequency, calling it $\theta_n(z,f)$. However, for our field observations, it is first necessary to project the measurements of $v_{x_i}(t)$ and $v_{y_i}(t)$ (each being complex) into a single horizontal particle velocity v_{r_i} using

$$v_{r_i} = v_{x_i}\cos(\phi_B - \phi_x) + v_{y_i}\cos(\phi_B - \phi_y) \tag{12}$$

where ϕ_x is the bearing of *x* channel, ϕ_y is the bearing of *y* channel, and ϕ_B is the bearing of IVAR from a particular SUS station. Knowing $v_{r_i}(t)$ and $v_{z_i}(t)$, the equation to estimate scalar circularity from field data reduces to

$$\theta_n(z_m, f_i) = \frac{2\ \mathrm{Im}\{v_{r_i}(t_n)v^*_{z_i}(t_n)\}}{|v_{r_i}(t_n)|^2 + |v_{z_i}(t_n)|^2}. \tag{13}$$

A model for $\theta_n(z,f)$ emerges by using previously derived model values for V_{r_n} and V_{z_n} as follows:

$$\theta_n(z,f) = \frac{2\ \mathrm{Im}\{V_{r_n}V^*_{z_n}\}}{|V_{r_n}|^2 + |V_{z_n}|^2}. \tag{14}$$

D. Normalized Vertical Reactive Intensity $Q^\star_{z_n}(z,f)$

The vertical component of reactive intensity was introduced [see Fig. 6(d)]. D'Spain *et al.* [14] explain the significance of vector quantity $\vec{Q}$ by multiplying the equation for conservation of momentum by pressure and then operating in the spectral domain. It is useful to provide here a small variation on this development; keeping in the time domain and using the Hilbert transformed variables (see Section III) yields

$$i2\pi f\rho\ p\vec{v^*} + p\nabla p^* = 0. \tag{15}$$

Assuming a spatial dependence in p going as $|p(x,y,z))|\ e^{i\phi(x,y,z)}$ gives

$$\pi f\rho\vec{Q} + i\pi f\rho\vec{I} + |p|\nabla|p| + i|p|^2\nabla\phi = 0 \tag{16}$$

and after equating real and imaginary parts and dividing by $|p|^2$, we obtain the desired result as

$$\rho c_w\frac{\vec{Q}}{|p|^2} = \frac{\nabla|p|^2\lambda}{4\pi|p|^2} \tag{17}$$

with the interpretation that reactive intensity normalized by a scalar intensity gives the fractional change of field magnitude squared per unit wavelength [14].

Normalizing reactive intensity $\vec{Q}$ by a scalar intensity $(|p|^2/\rho c_w)$ removes the range dependence and provides advantages because important properties emerge in regions of low signal level (see the research work by Dall'Osto *et al.* [21]). We refer to this normalized quantity as $\vec{Q}^\star$ (where the star symbol identifies this as a normalized quantity and should not be confused with the complex conjugation.) The immediate focus in this paper is on the vertical component of $\vec{Q}^\star$, which, as in the above metrics, is defined here as the function of mode number, measurement depth, and frequency, or $Q^\star_{z_n}(z,f)$. From field data, we estimate $Q^\star_{z_n}(z,f)$ as

$$Q^\star_{z_n}(z_m, f_i) = \rho c_w\frac{Q_{z_i}(t_n)}{|p_i(t_n)|^2} \tag{18}$$

and a model for $Q^\star_z(z,f)$ using the previously derived single-mode pressure and particle velocity as a function of frequency is

$$Q^\star_{z_n}(z,f) = \rho c_w\frac{\mathrm{Im}\{P_nV^*_{z_n}\}}{|P_n|^2}. \tag{19}$$

Note the behavior of $Q^\star_{z_n}(z_m, f_i)$ and $\theta_n(z_m, f_i)$ and corresponding models will be similar, as anticipated from the numerators of (14) and (19), both of which govern the sign change. That is, given that the radial particle velocity $v_{r_i(t)}$ and pressure $p_i(t)$ are likely to be nearly exactly in phase for the active field then $Q^\star_{z_n}(z_m, f_i)$, which is based on the latter, will have similar behavior. However, each provides an independent examination of the data, because the denominator of $\theta_n(z_m, f_i)$ includes both horizontal and vertical components of particle velocity and this quantity is bound by ±1, whereas that of $Q^\star_{z_n}(z_m, f_i)$ is based on pressure and can assume extreme values, especially when evaluated near complicated multimode interference structures [21].

E. Comparison of Model Results Based on Two Geoacoustic Models

Model results for the four quantities derived from the vector acoustic measurements are compared using two different geoacoustic representations (or geoacoustic models), the first being a notional one for the SBCEX experimental conditions corresponding to the IVAR location and the second being a half-space, or Pekeris representation (see Table I). We emphasize that the notional geoacoustic model is not a result of an inversion *per se* but instead meant as a nominally consistent representation of available ground truth data in terms of water depth measured at IVAR (mean depth, 74.4 m), measured water sound speed c_w, and approximate mud-layer thickness at the IVAR site based high-resolution chirp acoustic reflection data [1]. Some experimentation with forward modeling is required to establish parameters for the mud layer, a key component of the notional geoacoustic model, and we use values consistent with those emerging from recently published studies [2], [4], such as mud-layer thickness and linear sound-speed gradient equal to $10\ \mathrm{s}^{-1}$.

TABLE I
SUMMARY OF GEOACOUSTIC REPRESENTATIONS

Notional SBCEX	Layer Thickness	Sound Speed	Density	Attenuation
Water	74.4 m	1468.3 m/s	1027 kg/m^3	0 dB/λ
Mud	11 m	1445-1555 m/s	1600 kg/m^3	0.05 dB/λ
Halfspace	semi-infinite	1830 m/s	2000 kg/m^3	0.25 dB/λ
Pekeris	Layer Thickness	Sound Speed	Density	Attenuation
Water	74.4 m	1468.3 m/s	1027 kg/m^3	0 dB/λ
Halfspace	semi-infinite	1830 m/s	2000 kg/m^3	0.25 dB/λ

We first undertake a brief analysis of sediment attenuation to confirm that the attenuation parameters (see Table I) are at least nominally consistent with the data. For a given source station, active horizontal intensity for modes $n = 1, 2, 3$ and frequency indices f_i between about 15 and 60 Hz (depending on mode) is taken to be $\sqrt{I^2_{x_i}(t_n) + I^2_{y_i}(t_n)}$. For example, for the SUS station S45 at range 10 km [see Fig. 6(e)], active horizontal intensity is dominated by the y-component and $I_{y_i}(t_n)$ at 30 Hz for modes 1 and 2 are 0.05 and 0.13 mW/m^2, respectively.

Data from all stations studied (see Fig. 3) are collected in this manner, and we assume these data take on a range behavior embodied by $|A_n|^2$, which will have the range dependence going as $e^{-2\mathrm{Im}\{k_n\}R}/R$. The cylindrical spreading term is removed, and what remains is the decay for a particular mode governed by the imaginary part of the modal horizontal wave number $k_n(f_i)$. For example, the entire set of active horizontal intensity data for mode 2, 30 Hz (see Fig. 7 inset) is fitted to a single curve, with cylindrical spreading built in, and an estimate of $\mathrm{Im}\{k_n(f_i)\}$ is then derived from this curve fit (solid line in Fig. 7 inset). Results for the first three modes (see Fig. 7) show that the imaginary part of the horizontal wave number increases rapidly near the cutoff of the mode, and then assumes a more constant value. Admittedly, this is a delicate operation on the data with results susceptible to interference effects. Nonetheless, the analysis confirms that $\mathrm{Im}\{k_n\}$ values derived from the notional SBCEX geoacoustic model based on less attenuation in the mud layer than in the sediment half-space (see Fig. 7, solid, black lines) are reasonably consistent.

More detail is required to describe sediment attenuation properly. For now, we accept this deficiency in our notional SBCEX geoacoustic model given its purpose in this paper, with the results (see Fig. 7) motivating a more refined inversion on sediment attenuation. Finally, we note that this analysis can also be undertaken using potential energy $E_{p_i}(t_n)$ measured as a function of range based on a single pressure sensor (thick, dotted lines in Fig. 7). These results are in agreement with those derived from active horizontal intensity with the exception of mode 1, which covers a much lower frequency range. Here signal-to-noise limitations that affect the pressure and velocity channels differently can be an issue.

Based on the geoacoustic data in Table I, we compute, as a function of frequency for modes 1–4, model results (see Fig. 8) for depth-dependent mode speed of energy $u_{e_n}(z, f)$ (10), circularity $\theta_n(z, f)$ (14), and normalized vertical reactive intensity $Q^{\star}_{z_n}(z, f)$ (19). Also coming directly from the normal mode calculations are phase speed $v_{p_n(f)}$ and group speed $v_{g_n(f)}$, for which the latter, although not included in the four quantities to be derived from the vector acoustic measurements, will be interesting to include.

The different behaviors for $u_{e_n}(z, f)$, $\theta_n(z, f)$, and $Q^{\star}_{z_n}(z, f)$ based on notional SBCEX and Pekeris models are striking, and suggests that these quantities, when in the form of reliable field data, have great potential to resolve information about the seabed. When based on the notional SBCEX model, both $\theta_n(z, f)$ and $Q^{\star}_{z_n}(z, f)$ also undergo a change in sign for mode 2 at 37 Hz, whereas when based on the Pekeris model, the sign change for mode 2 occurs very close to, if not precisely at, the cutoff frequency for mode 2, which is approximately 25 Hz. In terms of the parameters given in Table I, the mud-layer thickness combined with the average compressional wave speed within this layer appears to have the greatest controlling influence on this property.

V. RESULTS

Experimental values (see Fig. 9) are presented for the mode- and frequency-dependent vector acoustic quantities (see Sections IV-A–IV-D) , based on observations from 22 SUS stations (see Fig. 3) for which the range to IVAR exceeds 5 km and there is sufficient dispersion to identify separate mode arrivals (see Fig. 6(a)]. Additionally, the modal group speed $v_{g_n}(f_i)$ is estimated directly from the time–frequency address locations generated from E_p for any arrival [see Fig. 6(a)]. Given the known range R between SUS detonation and IVAR and water sound speed c_w, $v_{g_n}(f_i) = R/t$, where $t = t_0 + \Delta t$ is the total travel time, with Δt established by the time–frequency address and $t_0 = R/c_w$ is the arrival time of the broadband peak.

Each quantity has 110 independent estimates, based on the five SUS detonations for a given station (range) and 22 stations used in this analysis. As a measure of central tendency and to avoid undue influence of outliers, we use the median value

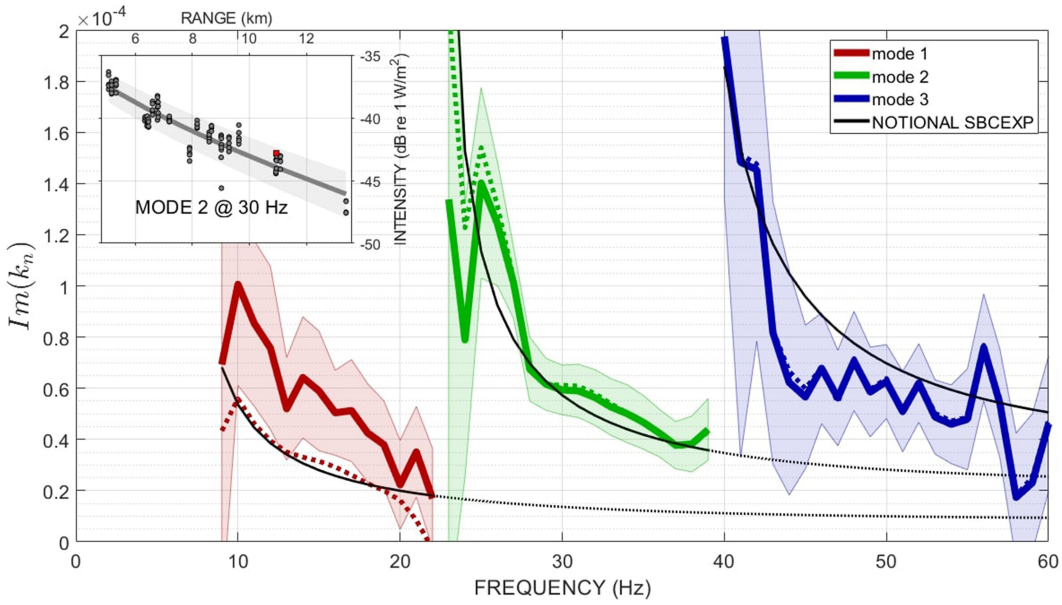

Fig. 7. Imaginary part of horizontal wave number k_n for modes $n = 1, 2, 3$ as derived from analysis of horizontal intensity from SUS arrivals measured at the IVAR site, ranges 5–13 km. Thicker color-coded solid lines represent the median estimate of $\mathrm{Im}\{k_n\}$ as a function of central frequency f_i, with shading bracketing the 95th percentile range. Color-coded dotted lines are equivalent estimates based on potential energy (see text) that align with those based on horizontal intensity with exception of mode 1. Solid, black lines are values $\mathrm{Im}\{k_n\}$ from the Kraken normal mode program upon using the attenuation values in Table I. Inset: Example of active horizontal intensity as function of range for mode 2 and central frequency 30 Hz. Thick line is fitted curve from which estimates of $\mathrm{Im}\{k_n\}$ are derived.

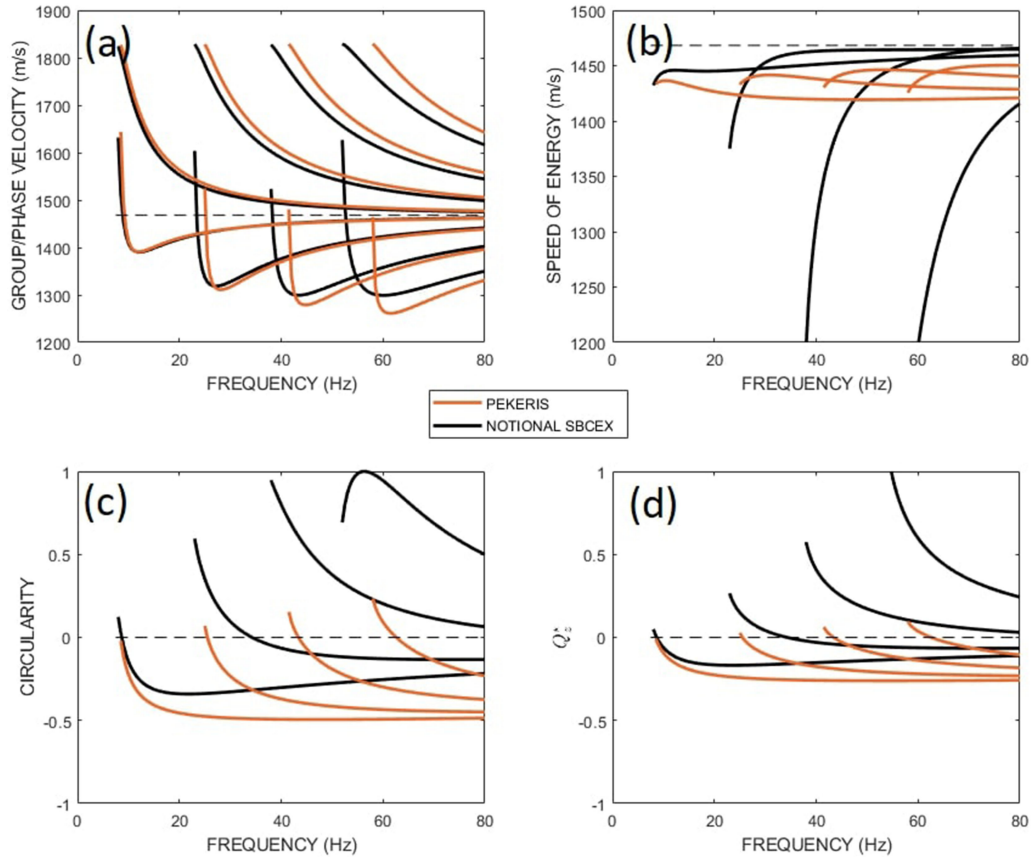

Fig. 8. Theoretical predictions for the four vector acoustic quantities plus group speed, based on the two geoacoustic models in Table I. (a) Phase speed $v_{p_n}(f)$ (above the horizontal dashed line c_w) and corresponding group speed $v_{g_n}(f)$. (b)–(d) Depth-dependent vector acoustic quantities evaluated at IVAR depth: (b) mode speed of energy $u_{e_n}(z, f)$ with horizontal dashed line equal to c_w, (c) scalar circularity $\theta_n(z, f)$, and (d) vertical component of reactive intensity normalized by scalar intensity $Q^{\star}_{z_n}(z, f)$

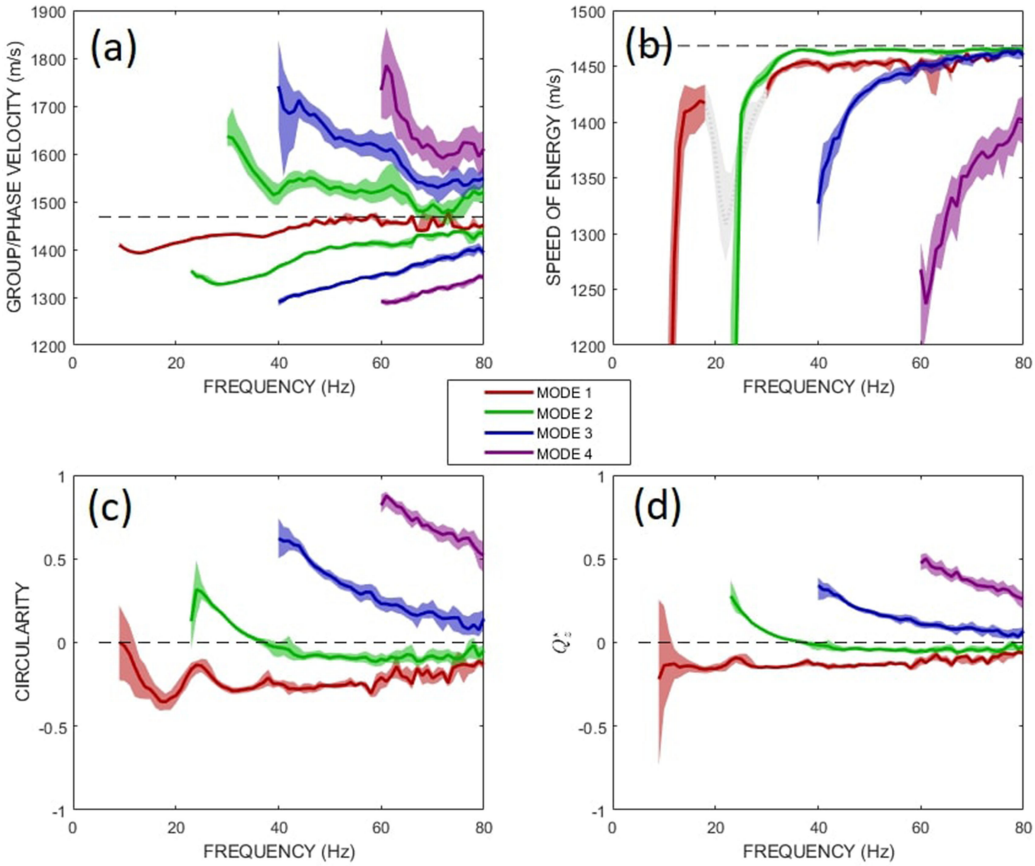

Fig. 9. (a) Experimental values of phase speed $v_{p_n}(f_i)$ (above the horizontal dashed line) and group speed $v_{g_n}(f_i)$ (below the dashed line). (b) Mode speed of energy $u_{e_n}(z_m, f_i)$. (c) Scalar circularity $\theta_n(z_m, f_i)$. (d) Vertical component of reactive intensity normalized by scalar intensity $Q^{\star}_{z_n}(z_m, f_i)$.

as the final estimate (thick lines in Fig. 9) with uncertainty characterized by the 25th (lower bound) and 75th percentiles.

Group speed estimates based on the pressure channel [see Fig. 9(a)] suggest a frequency of the Airy phase for mode 2 at 28 Hz, which is in agreement with that recently reported by Wan *et al.* [4]; additionally, we report an Airy phase group speed for mode 2 equal to 1328 m/s (median), with a 25th–75th percentile range of 1326–1333 m/s. However, signal-to-noise limitations prevented estimates of the Airy phase for modes 3 and 4. The Airy phase of mode 1 has a frequency of 13 Hz and speed 1393 m/s with 25th–75th percentile equal to 1392–1396 m/s. The estimates of group speed are from varying angular sectors (see Fig. 3) and thus necessarily represent a range average over differing mud thicknesses [1], see also [4, Fig. 1], yet the bounds on these estimates are reasonably tight. This observation is anticipated based on the results from the notional geoacoustic model [see Fig. 8(a)], for which group velocities (black lines) are consistent with our experimental values for mode 1 and mode 2; however, these results are expected to shift little by changing the mud-layer thickness a meter or two because the Pekeris model yields similar results.

For estimates of phase speed $v_{p_n(f)}$ [estimates located above the dashed line equal to c_w in Fig. 9(a)], variation about the median for any given frequency is greater and a reliable estimate of mode 1 phase speed is not possible, although the phase speed estimates obtained are reasonably comparable with those from the notional geoacoustic model [see Fig. 8(a)]. As with group speed, model estimates of phase speed also show considerable similarity between the two widely different geoacoustic models, particularly for modes 1 and 2, and we anticipate that these observations offer a lower measure of information about the seabed.

The three quantities relating to individual-mode frequency-dependent estimates of the mode speed of energy [see Fig. 9(b)], circularity [see Fig. 9(c)], and normalized vertical reactive intensity [see Fig. 9(d)], all of which are depth dependent, present an interesting collective case. Inspecting their patterns versus frequency and mode number suggests that there is information in these data that motivates resolving more than a half-space, or Pekeris, representation for a geoacoustic model, and that something like the notional geoacoustic model (see Table I) is required. At this point, we postpone a formal geoacoustic inversion to future work or to works by other researchers studying these data.

However, a key property of mode 2 as observed at the IVAR location is the zero crossing near 37 Hz for estimates of $\theta_n(z_m, f_i)$ [see Fig. 9(c)] and $Q^{\star}_{z_n}(z_m, f_i)$ [see Fig. 9(d)]; any geoacoustic model that originates from this experiment ought to exhibit this property in mode 2 when applied to the IVAR location (depth 74.4 m). Thus, we posit this value as a constraint observation for mode 2, with formal median value of 37.3 Hz and 25th–75th percentile range of 36–39 Hz.

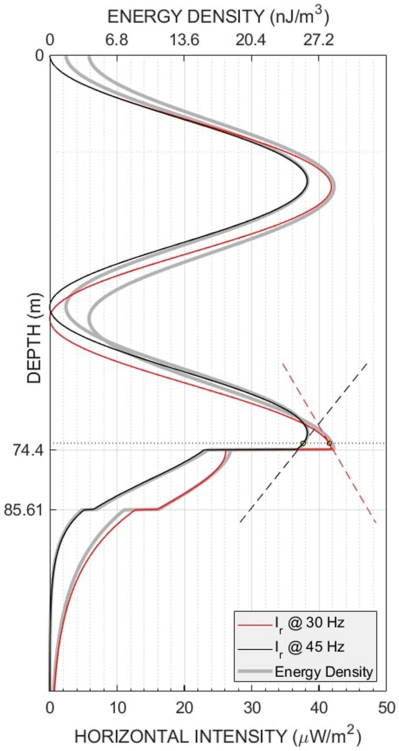

Fig. 10. Horizontal intensity for mode 2 at 30 Hz (red) and 45 Hz (black) assuming the notional SBCEX geoacoustic model (see Table I) combined with true measurements made at the IVAR measurement depth (horizontal dotted line). Energy densities (thick gray lines) follow closely the corresponding horizontal intensities as seen by the overlapping lines, which separate toward the sea surface. Two slope indicators (short, dashed lines) indicate the sign of the vertical derivative of the pressure magnitude squared at the IVAR measurement depth.

To further understand this property, we examine the behavior of mode 2 at two frequencies that span 37 Hz (see Fig. 10) based on the notional SBCEX geoacoustic model (see Table I). Take for purposes of demonstration, values for energy density $E_{p_i}(t_n) + E_{k_i}(t_n)$ and horizontal intensity $\sqrt{I^2_{x_i}(t_n) + I^2_{y_i}(t_n)}$ observed at the IVAR measurement depth z_m for mode 2 at 30 Hz and 45 Hz, as can be inferred from Fig. 6(a)–(c), noting in this case $I_{x_i}(t_n) \approx 0$. Using the notional SBCEX geoacoustic model, we compute $U_n(z)$ and k_n for $n = 2$ at 30 and 45 Hz and derive an estimate of $|A_n|^2$ for $n = 2$ at these frequencies by equating the measured to theoretical values of horizontal intensity I_r, where

$$I_r = \frac{|A_n|^2 \mathrm{Re}\{k_n\}|U_n(z)|^2}{2\pi f \rho(z)}. \tag{20}$$

Using (20), I_r may now be extrapolated over the entire water column and sediment depth where we require a depth-dependent density $\rho(z)$. An analogous operation is applied to energy density, with both I_r and $E_p + E_k$ as functions of depth shown for mode 2 at frequencies 30 and 45 Hz (see Fig. 10).

Returning to the original issue of the zero crossing, take I_r as surrogate for $|p|^2$ as used in (17) to demonstrate how reactive intensity relates to the gradient of the pressure magnitude squared. The vertical derivative of I_r changes sign at the IVAR measurement depth between frequencies 30 and 45 Hz (see slope indicators, Fig. 10) and equals 0 at approximately 37 Hz, which explains the behavior in $Q^{\star}_{z_n}(z_m, f_i)$. Similarly, on a single-mode basis, pressure and horizontal particle velocity are in phase, and therefore estimates of scalar circularity behave like $Q^{\star}_{z_n}(z_m, f_i)$ in terms of the sign change property for mode 2. (Observe that I_r can be discontinuous across the water–sediment boundary, whereas I_z will be continuous [23].)

Estimates for the modal speed of energy [see Fig. 9(b)], which assume seemingly nonintuitive values [i.e., resembling nothing like the phase or group speeds shown in Figs. 8(a) and 9(a)], mirror the estimates based on the notional SBCEX model [see Fig. 8(b)]. Over frequencies 30–45 Hz, estimates for the speed of energy for mode 2 vary smoothly from ∼1442 m/s to ∼1465 m/s, which is slightly less than the c_w value and there are similar changes observed for modes 1, 3, and 4 but over different frequency ranges.

VI. Summary and Additional Remarks

The IVAR is a system that records four coherent channels of acoustic data continuously: one channel for acoustic pressure and three channels associated with a triaxial accelerometer from which acoustic particle velocity is obtained. Using the IVAR, the vector acoustic field of broadband signals originating from SUS (Mk-64) charges deployed at ranges 5–13 km from the fixed IVAR site (mean depth 74.4 m) were studied as part of the 2017 SBCEX relating to the study of the acoustics of fine-grained muddy sediments. Sufficient geometric dispersion at these ranges permitted unambiguous identification of up to four modes as a function of frequency in the range ∼15–80 Hz.

From the time–frequency analysis of the dispersed arrivals, time–frequency addresses of single-mode (n) and single-frequency (f_i) arrivals are identified. Four vector acoustic quantities are estimated at each address: first, mode phase speed $v_{p_n}(f_i)$; second, depth-dependent mode speed of energy $u_{e_n}(z_m, f_i)$; third, scalar circularity $\theta_n(z_m, f_i)$; and fourth, normalized vertical reactive intensity $Q^{\star}_{z_n}(z_m, f_i)$, for which the last three depend on the IVAR measurement depth z_m of 1.25 above the seafloor. In addition, modal group speed $v_{g_n(f_i)}$ is estimated directly from the dispersed arrivals measured on the pressure channel.

A comprehensive feature of these observations, measured at ranges 5–13 km, is the general collapse onto a single curve as a function of frequency for a given mode, although some better than others. This implies that these data represent a measure of the local mode properties as realized at the IVAR site; the observations of group speed are an exception in that they represent an average group speed for the SBCEX experimental area at the particular measurement range [2].

The observations are easily modeled using a normal mode-based propagation code providing a pathway for geoacoustic inversion. A comparison of observations with model results, with the latter based on: first, a notional geoacoustic representation for the SBCEX experimental area consisting of single low-speed mud layer over a half-space, and second, a Pekeris representation based on the same half-space (see Table I), shows striking differences (see Fig. 8). The field observations (see Fig. 9) are clearly at variance with the Pekeris representation. The notional

geoacoustic representation is designed to be consistent with available ground truth and incorporate sediment attenuation parameters based on experimental results on the range decay of identifiable mode arrivals to estimate $\mathrm{Im}\{k_n\}$. Beyond this, a formal inversion to assess more quantitatively the resolving power of these data, for example, the ability to resolve sound-speed gradients, or additional granularity in sediment layering, requires further study.

Nonetheless, the notional geoacoustic representation for the SBCEX experimental area does provide some guidance. In particular, mode properties emerging from it predict well the zero crossing near 37 Hz for mode circularity [see Fig. 8(c)] and normalized vertical reactive intensity [see Fig. 8(d)]. This effect is manifested in observations of $\theta_n(z_m, f_i)$ and $Q^{\star}_{z_n}(z_m, f_i)$ in the form of a zero crossing and change in sign, a property that is observed consistently in more than 100 observations based on the 5–13 km source range set. It is a fundamental feature of the mode structure as realized at the IVAR site that cannot be reproduced in the absence of a low-speed, mudlike layer.

Finally, although it is demonstrated that information content in $u_{e_n}(z_m, f_i)$, $\theta_n(z_m, f_i)$, and $Q^{\star}_{z_n}(z_m, f_i)$ as data measures for geoacoustic inversion appears to be high, they are not sensitive to sediment attenuation. Note that this insensitivity is a feature of the single-mode representation of these quantities, and then for a field subject to multimode interference, range dependence and sensitivity to attenuation likely would be exhibited. However, our analysis of active horizontal intensity as a function of mode and frequency for all ranges to obtain estimates of $\mathrm{Im}\{k_n\}$ suggests that much less attenuation in the mud layer than in the sediment half-space (see Table I) is required to be compatible with observations. It is possible that other vector acoustic quantities, such as active vertical intensity or reactive horizontal intensity, will be of greater use as a measure of sediment attenuation, and furthermore not require observations over range. This, too, will be assessed in future work.

ACKNOWLEDGMENT

The authors would like to thank the crew of *R/V Endeavor* for carrying out a successful deployment and recovery of the IVAR in heavy seas, D. Knobles and P. Wilson for their excellent planning of SUS charge sources, and the Naval Surface Warfare Center for operation of the explosive charges. They would also like to gratefully acknowledge the efforts of all SBCEX participants.

REFERENCES

[1] J. A. Goff, A. H. Reed, G. Gawarkiewicz, P. S. Wilson, and D. P. Knobles, "Stratigraphic analysis of a sediment pond within the New England Mud Patch: New constraints from high-resolution chirp acoustic reflection data," *Mar. Geol.*, to be published.

[2] J. Bonnel *et al.*, "Geoacoustic inversion on the New England Mud Patch using warping and dispersion curves of higher-order modes," *J. Acoust. Soc. Amer.*, vol. 143, pp. EL405–EL411, 2018.

[3] C. B. Leslie, J. M. Kendall, and J. L. Jones, "Hydrophone for measuring particle velocity," *J. Acoust. Soc. Amer.*, vol. 28, pp. 711–715, 1956.

[4] L. Wan, M. Badiey, D. P. Knobles, and P. S. Wilson, "The airy phase of explosive sounds in shallow water," *J. Acoust. Soc. Amer.*, vol. 143, pp. EL199–EL205, 2018.

[5] L. M. Brekhovskikh, *Waves in Layered Media*. New York, NY, USA: Academic Press, 1960.

[6] N. R. Chapman, "Measurement of the waveform parameters of shallow explosive charges," *J. Acoust. Soc. Amer.*, vol. 78, pp. 672–681, 1985.

[7] F. J. Fahy, *Sound Intensity*, 2nd ed. London, U.K.: Chapman & Hall, 1995.

[8] R. C. Heyser, "Instantaneous intensity," in *Proc. 81st Conv. Audio Eng. Soc.*, Los Angeles, CA, USA, Nov. 12-16, 1986, Art. no 2399.

[9] F. Jacobsen, "A note on instantaneous and time-averaged active and reactive intensity," *J. Sound Vib.*, vol. 147, pp. 489–496, 1991.

[10] J. A. Mann III, J. Tichy, and A. J. Romano, "Instantaneous and time averaged energy transfer in acoustic fields," *J. Acoust. Soc. Amer.*, vol. 82, pp. 17–30, 1987.

[11] F. Jacobsen, "Active and reactive, coherent an incoherent sound fields," *J. Sound Vib.*, vol. 130, no. 3, pp. 493–507, 1989.

[12] M. B. Porter and E. L. Reiss, "A numerical method for ocean acoustic normal modes," *J. Acoust. Soc. Amer.*, vol. 76, pp. 244–252, 1984.

[13] F. B. Jensen, W. A. Kuperman, M. B. Porter, and H. Schmidt, *Computational Ocean Acoustics*, 2nd ed. New York, NY, USA: Springer, 2011.

[14] G. L. D'Spain, W. S. Hodgkiss, and G. L. Edmonds, "Energetics of the deep oceans infrasonic sound field," *J. Acoust. Soc. Amer.*, vol. 89, pp. 1134–1158, 1991.

[15] G. Schiffrer and D. Stanzial, "Energetic properties of acoustic fields," *J. Acoust. Soc. Amer.*, vol. 96, pp. 3645–3653, 1994.

[16] I. Tolstoy, "Resonant frequencies and high modes in layered waveguides," *J. Acoust. Soc. Amer.*, vol. 28, pp. 1182–1192, 1956.

[17] A. Pierce, "The natural reference wavenumber for parabolic approximations in ocean acoustics," *Comput. Math. Appl.*, vol. 11, pp. 831–841, 1985.

[18] V. A. Shchurov, *Vector Acoustics of the Ocean.* Vladivostok, Russia: Dalnauka, 2006.

[19] D. R. Dall'Osto, J. W Choi, and P. H. Dahl, "Measurement of acoustic particle motion in shallow water and its application to geoacoustic inversion," *J. Acoust. Soc. Amer.*, vol. 139, pp. 311–319, 2016.

[20] D. R. Dall'Osto and P. H. Dahl, "Observations of water column and bathymetric effects on the incident acoustic field associated with shallow water reverberation experiments," *IEEE J. Ocean. Eng.*, vol. 42, no. 4, pp. 1146–1161, Oct. 2017.

[21] D. R. Dall'Osto, P. H. Dahl, and J. W. Choi, "Properties of the acoustic intensity vector field in a shallow water waveguide," *J. Acoust. Soc. Amer.*, vol. 131, pp. 2023–2035, 2012.

[22] D. R. Dall'Osto and P. H. Dahl, "Elliptical particle motion in underwater waveguides," *J. Acoust. Soc. Amer.*, vol. 134, pp. 109–118, 2013.

[23] D. M. F. Chapman, "Using streamlines to visualize acoustic energy flow across boundaries," *J. Acoust. Soc. Amer.*, vol. 124, pp. 48–56, 2008.

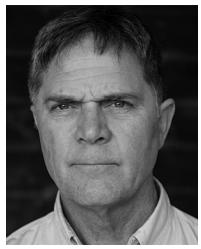

Peter H. Dahl (M'02–SM'17) received the Ph.D. degree in ocean engineering from the Massachusetts Institute of Technology, Cambridge, MA, USA/Woods Hole Oceanographic Institution, Woods Hole, MA, USA, Joint Program in Oceanography and Oceanographic Engineering, in 1989.

He is currently a Senior Principal Engineer with the Applied Physics Laboratory, University of Washington, Seattle, WA, USA, and a Professor in mechanical engineering with the University of Washington. His research interests include experimental and modeling studies on intensity vector acoustics, the influence of sea surface conditions on underwater sound propagation and reverberation, and studies on the underwater sound field from pile driving and explosive sources.

Dr. Dahl is a Fellow of the Acoustical Society of America (ASA). He was the Chair for the ASA Technical Committee on Underwater Acoustics and the ASA Executive Council and the ASA Vice-President (2013–2014.) He was a Chief Scientist on *R/V Endeavor* (Leg 1) during the Office of Naval Research Seabed Characterization Experiment.

David R. Dall'Osto received the Ph.D. degree in mechanical engineering from the University of Washington, Seattle, WA, USA, in 2013.

He is currently a Senior Research Scientist and Engineer with the Applied Physics Laboratory, University of Washington. His research interests include modeling and measurement of acoustic intensity in the ocean and atmosphere, on both short-range and global scales. An important aspect of his research is the discovery of physical processes that produce structure in the intensity vector field and validating such theoretical predictions through experiment.

Range-Dependent Inversion for Seabed Parameters Using Vector Acoustic Measurements of Underwater Ship Noise

Peter H. Dahl, *Senior Member, IEEE*, and David R. Dall'Osto

***Abstract*—The Intensity Vector Autonomous Recorder (IVAR) measures acoustic particle velocity and pressure simultaneously. IVAR was deployed on the seabed during the 2017 Seabed Characterization Experiment (SBCEX) with the primary objective to study sound propagation within underwater waveguides for which the seabed consists of fine-grained, muddy sediments. In this study, a Bayesian framework is applied to underwater noise recorded by IVAR from a cargo ship traversing the central region of the SBCEX2017 area for the purpose of inversion to characterize sediment properties. The vector acoustic data are in the form of a bounded, nondimensional form known as circularity, a quantity that is independent of the ship noise-source spectrum and that can be interpreted as the normalized curl of active intensity. The inversion model space for the seabed consists of a low-compressional speed layer and underlying basement half-space, with each having compressional and shear components. The interpretative model for producing a replica of the data is based on the plane wave reflection coefficient for a layered, elastic seabed in conjunction with the depth-dependent Green's function that is integrated in the complex wave number plane to obtain pressure and particle velocity fields. The small change in water depth between the location of the ship source and IVAR is addressed using adiabatic mode theory. The inversion results exhibit slow variation over the 20-min observation period, representing approximately 5 km of travel by the ship source.**

***Index Terms*—Acoustic particle velocity, active intensity, circularity, reactive intensity, vector acoustics.**

I. Introduction

THE Seabed Characterization Experiment (SBCEX2017) was conducted in March–April 2017 over an approximate 10×30 km seabed area known as the New England mud patch, located about 95 km south of Cape Cod, MA, USA. The primary objective of SBCEX2017 is centered on the physics of sound propagation in fine-grained, muddy sediments. Study elements included the inversion of acoustic observations to characterize sediment properties, sediment coring, sub-bottom profiling, and stratigraphic analysis. A large fraction of the experimental area is distinguished by a layer of fine-grained sediment of order 10-m-thick starting at the water–sediment interface and upper sediment sound speed close to the water sound speed at the water–sediment interface. Results from several SBCEX2017 studies are summarized in [1].

In this study, vector acoustic properties of underwater noise from a cargo ship traversing the central region of the SBCEX2017 area are inverted for sediment characteristics using a Bayesian approach. The model space is restricted to describing a low-compressional and low shear-speed layer, and the underlying basement half-space with higher compressional and shear speeds. The observations were made with the Intensity Vector Autonomous Recorder (IVAR), a system that records four coherent channels of acoustic data continuously: one channel for acoustic pressure and three channels associated with a neutrally buoyant tri-axial accelerometer from which acoustic particle velocity is obtained. The system is described by Dahl and Dall'Osto [2] in relation to measurements from broadband SUS (Mk-64) explosive charges made during SBCEX2017.

This study expands upon results reported by Dahl and Dall'Osto [3], with the following key differences:

1) range dependence (in water depth) is addressed using an adiabatic approach;
2) a different, and arguably more comprehensive, vector acoustic measure, known as circularity, is used in the inversion;
3) a greater frequency range is employed in the inversion;
4) the inversion parameter set used here accommodates elastic features of the seabed, whereas a nonelastic seabed was modeled in the previous study.

This article is organized as follows. In Section II, the data, measurement period, and location are described, along with the means by which the estimates of circularity are derived from the vector sensor observations. Section III describes our approach to modeling circularity based on the depth-dependent Green's function, a model for the plane wave reflection coefficient for a layered, elastic seabed, and adiabatic constructions of complex fields. The geoacoustic inversion is described in Section IV, and results discussed in Section V. Finally, Section VI concludes this article.

Manuscript received January 29, 2019; accepted May 28, 2021. This work was supported by the U.S. Office of Naval Research, Code 32, Ocean Acoustics. *(Corresponding author: Peter H. Dahl.)*

Guest Editor: D. Knobles.

Peter H. Dahl is with the Applied Physics Laboratory and Department of Mechanical Engineering, University of Washington, Seattle, WA 98105 USA (e-mail: dahl@apl.washington.edu).

David R. Dall'Osto is with the Applied Physics Laboratory, University of Washington, Seattle, WA 98105 USA (e-mail: dallosto@apl.washington.edu).

Digital Object Identifier 10.1109/JOE.2021.3086880

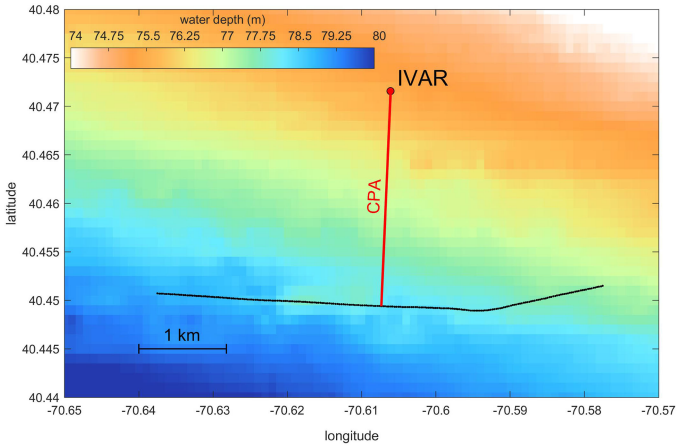

Fig. 1. Transit of *M/V Alice Oldendorf* ±10 min from the vessel's closet point of approach to IVAR as shown over the approximate bathymetry of the area. The vessel is moving east to west.

II. Observations of Underwater Ship Noise

Underwater noise originating from the transit of *M/V Alice Oldendorf* (IMO number 9183776, length 190 m) was recorded by IVAR on March 8. The vessel's closest point of approach (CPA) occurred at 21:23 UTC. At this time, the water depth at the IVAR location, 40.4716° N, 70.6061° W, was 75.5 m as measured by IVAR, and the vector acoustic measurements were made 1.25 m above the seafloor. Analyses are restricted to data recorded ±10 min about CPA (see Fig. 1) to exploit the higher signal level as the vessel was transiting approximately east to west at speed 8.2 kn. The CPA range, 2470 m, and speed are based on the ship's Automatic Identification System (AIS).

In the following analysis, the acoustic sample frequency is 5000 Hz, reduced via decimation from the initial sample frequency of 25 000 Hz for convenience, and data are expressed in the frequency domain, formulated by the Fourier transform of the pressure and three acceleration channels using a 1-s data Hanning window. One-sided complex spectra are retained, with each normalized to the variance of the corresponding time-domain data. This operation defines $S_p(f;t)$ as the complex spectrum for pressure and $S_{v_j}(f;t)$ for particle velocity, where f is the frequency and j represents the x, y, z components of velocity (upon division by $-i2\pi f$).

A 10-s moving-time average is taken on the squared spectral quantities, with the center-time value of this average retained establishing ΔT of 5 s for the time index (see also Section IV). For example, the potential energy density spectrum is $(1/2\rho c_w^2)\langle|S_p(f;t)|^2\rangle$, based on water density ρ of 1027.6 kg/m^3 and mean water sound speed c_w of 1470 m/s and with angle brackets denoting the average, and the kinetic energy density spectrum is $\frac{\rho}{2}\sum_{j=1}^{3}\langle|S_{v_j}(f;t)|^2\rangle$. A spectrogram [see Fig. 2(a)] of the potential energy density corresponding to the transit of *M/V Alice Oldendorf* past the CPA to IVAR, for the 20-min duration studied, shows the increased noise level received post-CPA, presumably owing to greater stern-aspect radiated noise. Time–frequency displays for this measure, the companion kinetic energy density, and the phase of cross-spectrum corresponding to an hour-long time span of the transit are shown in [3].

This study uses a nondimensional form of the data known as circularity $\Theta(t,f)$, which can be interpreted as the normalized curl of active intensity [4]. As in the case for the phase of the cross-spectrum used in [3], the estimates of circularity as a function of time and frequency are conveniently independent of ship source level. However, the estimates of $\Theta(t,f)$ also embody a greater degree of information concerning seabed properties than the data used in [3] because of, for example, greater sensitivity to multimode interference and more gradual change between extreme values of ± 1 that are better utilized in an inversion scheme.

Estimates of $\Theta(t,f)$ are computed by finding active I_j and reactive Q_j intensity components (averaged in the same manner)

$$I_j(f;t) = 0.5\langle \mathrm{Re}\{S_p(f;t)S_j^\star(f;t)\}\rangle \tag{1}$$

and

$$Q_j(f;t) = 0.5\langle \mathrm{Im}\{S_p(f;t)S_j^\star(f;t)\}\rangle. \tag{2}$$

Next, put

$$|I|^2(f,t) = \sum_{j=1}^{3} I_j^2 \tag{3}$$

and

$$|Q|^2(f,t) = \sum_{j=1}^{3} Q_j^2. \tag{4}$$

The two horizontal components (j = 1,2) are combined to estimate radial (or r-component) active and reactive intensity magnitude as follows $I_r(f,t) = \sqrt{I_1^2 + I_2^2}$ and $Q_r(f,t) = \sqrt{Q_1^2 + Q_2^2}$, and vertical components I_z, Q_z are associated with $j = 3$.

The estimate of circularity $\Theta(t,f)$ is thus given by [4]

$$\Theta(f;t) = 2\frac{I_r Q_z - I_z Q_r}{|I|^2 + |Q|^2}. \tag{5}$$

Equation (5) is a bounded indicator of the vector acoustic field (between ±1), taking on the maximum absolute value in the regions of destructive interference and shown to be effective in tracking the frequency dependence of waveguide interference features, including study of the waveguide invariant β [4]. Here, a scalar form is generated (by using I_r and Q_r) to allow comparison with a normal mode-based model for an underwater waveguide with cylindrical symmetry that supports only radial and vertical components of particle velocity. Thus, there is a small approximation in effect, insofar as I_r and Q_r can only be positive; however, instances where these can be negative occur in certain waveguide interference features that are spatially rare and have an extremely low signal level [5].

The estimate of $\Theta(f;t)$ [see Fig. 2(b)], like the potential energy density, also shows the characteristic interference pattern for the closing and opening about the CPA, but with added detail such as transition between modes. Approximate symmetry about the CPA is evident, with small deviations from symmetry that are

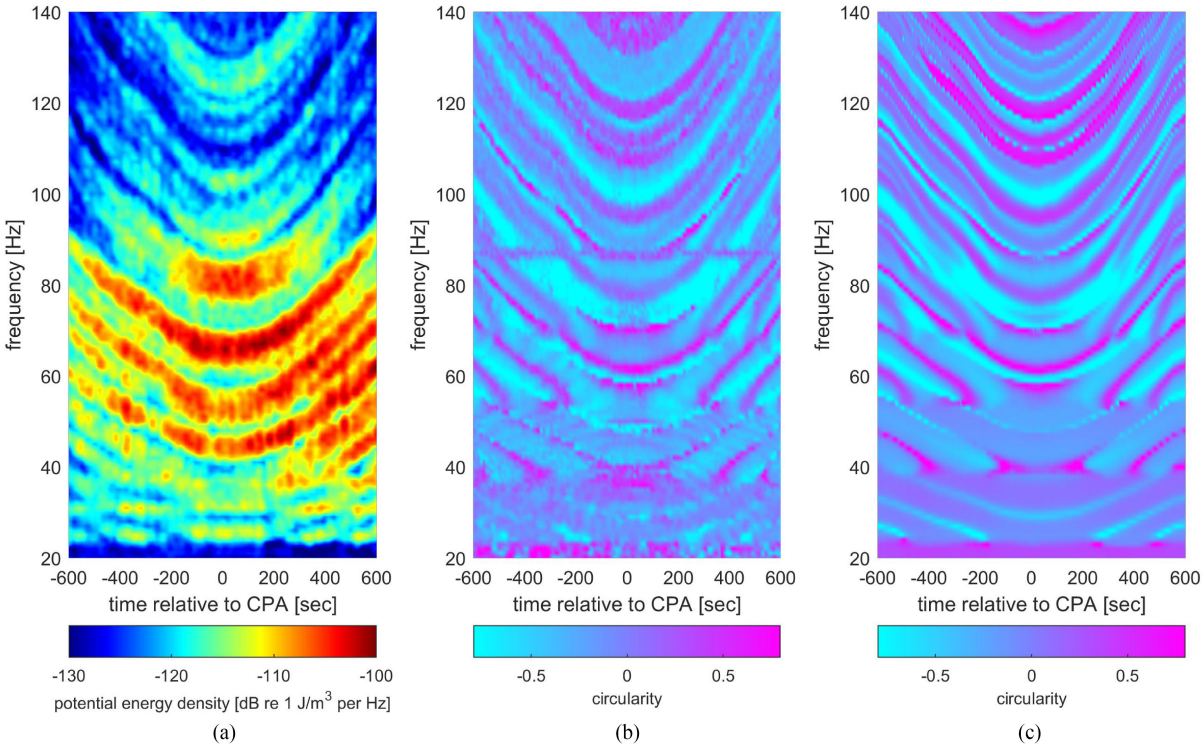

Fig. 2. (a) Potential energy density recorded during the transit of *M/V Alice Oldendorf* past the IVAR sensor. (b) Corresponding estimate of circularity (86–88-Hz band is corrupted by system noise). (c) Model replica of circularlity generated from a smoothed version of the inversion results, as discussed in Section V. Although the lowest frequency displayed is 20 Hz, data used in the inversion are limited to the frequency range 23–140 Hz.

postulated to be due to the slowly changing water depth under the vessel and changing bottom properties over the course of the transit.

Data over the frequency range 23–140 Hz, every 1 Hz, are used in the inversion [see Fig. 2(b)] with the exception of the 86–88-Hz band, which is corrupted by internal instrument noise, giving a total of 115 frequencies. The 1-Hz frequency spacing captures changes in the mode structure, with a smaller spacing increasing the dimensionality of the data with little or no advantage in the inversion. The lowest frequency of 23 Hz is on the very edge of reliable detection, owing to the receive bandwidth of IVAR (changed since 2017); we retain this frequency because of the interesting contrast between 23 and 24 Hz.

III. Forward Modeling

Following the methods of Dahl and Dall'Osto [3], the forward model used in the Bayesian inversion is based on a sum of normal modes for acoustic pressure and particle velocity. Here, however, we first obtain a model for the plane wave reflection coefficient for a layered, elastic seabed R_b, then use R_b in conjunction with the depth-dependent Green's function [6] that is integrated in the complex wave number plane to obtain pressure and particle velocity fields. Other more numerically based approaches can be used for this purpose, but this approach centered on finding R_b allows for an effective exploration of seabed parameter space that includes elastic properties.

A. Plane Wave Reflection Coefficient for a Layered Elastic Seabed Applicable to the SBCEX2017 Experimental Area

We compute the plane wave reflection coefficient R_b as a function of frequency for a sediment layer of thickness H overlying a half-space, with both layers including shear effects, following the matrix formulation of Vidmar and Foreman [7]. The physical model for the sediment [see Fig. 3(a)] is simplified from that used by Vidmar and Foreman, insofar as they allow sediment parameters within the layer to vary. The simplification to constant parameter values within the layer is because of the limited resolvability of our ship underwater noise data, e.g., it is not realistic to resolve gradients or other variation within layer H. The magnitude of R_b versus the grazing angle for the case of 120 Hz (solid line) is shown in Fig. 3(b), with sediment parameter values (representative of our final inversion results) used to generate R_b shown in Fig. 3(a). For comparison, the dotted line shows the case where shear effects are removed.

The characteristic function for finding modal eigenvalues k_n for water depth D satisfies

$$1 + R_b(k_n)e^{2i\gamma_n D} = 0 \tag{6}$$

where γ_n is the corresponding vertical wave number in the water column. Given the frequency range 23–140 Hz, searching for the roots of (6) is facilitated by using a starting seed value for k_n based on assimilating the acoustically transparent mud layer into the water column, giving a new water depth of $D + H$. The basement shear is temporarily ignored for this purpose (but not

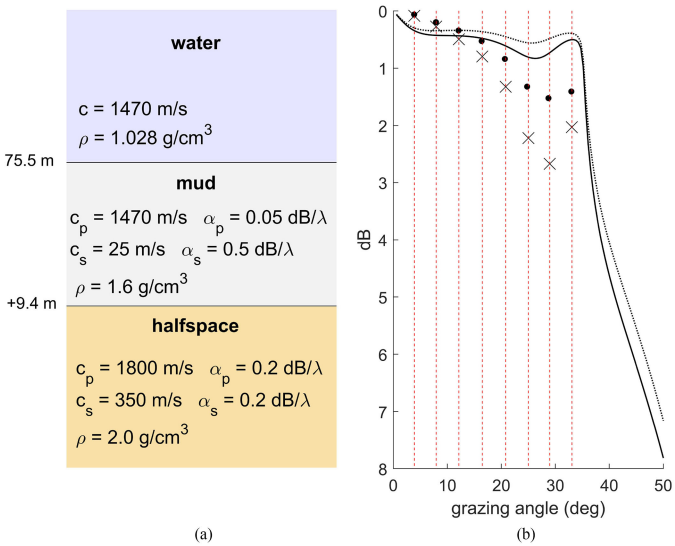

Fig. 3. (a) Physical model of the sediment for computing the plane wave reflection coefficient R_b. (b) Magnitude of R_b (solid line) in terms $-20\log_{10}|R_b|$, versus the grazing angle for the case of 120 Hz based on the parameters shown in (a). The dotted line shows the case when elastic parameters are set to 0. Dashed vertical lines show the equivalent grazing angles for the eight trapped modes. Loss for given modes (upon interpreting the y-axis in dB/km) are shown by the "X" symbol, with dots representing the case with elastic parameters set to 0.

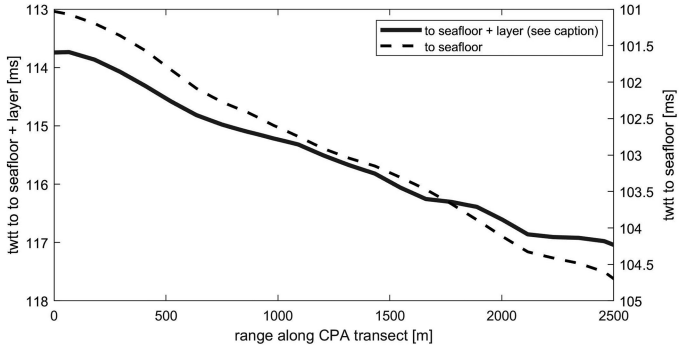

Fig. 4. Two-way travel times along the CPA transect shown in Fig. 1 to seafloor (dashed line) and to transition between the low-speed sediment layer and higher speed sediments (solid line). These data are parsed from structure maps of two-way travel time measurements for the seafloor and seabed interfaces by Goff *et al.* [10]. Range 0 represents the IVAR location; although not essential in current analysis, exact equivalence to 75.5 m requires a slightly higher sound speed in effect during the travel time measurements.

compressional attenuation) and the method in [8] is used to find an approximate k_n for a seed value, after which further iterations on (6) commence, leading to the final estimate of k_n. This search method is applied to both trapped and leaky modes.

The roots of (6) are complex wave numbers k_n that embody the propagation angle of the modes and the losses incurred with range exceeding cylindrical spreading. Equivalent grazing angles $\cos^{-1}\mathrm{Re}\{k_n\}/k$, where k is the corresponding wave number for a given frequency, for the eight trapped modes at 120 Hz fall on the plateau of the reflection coefficient [the dashed vertical lines in Fig. 3(b)]. The imaginary part of k_n [see Fig. 3(b)] is quantified as a loss in dB/km equal to $20\log_{10}[\exp(-\mathrm{Im}(k_n)1000)]$, where the x-symbols are for the case with seabed parameters as shown and dots are for the case where shear effects are removed. The loss per km for each mode generally increases with mode number, with greater loss for the elastic case, as expected. However, the presence of the shear layer also produces a rebound in the reflection coefficient at some frequencies. Note that the loss per km for the ninth mode, which is leaky, is about 20 dB/km and not shown on this plot. These effects, as manifested, in any given R_b as a function of frequency are subtle, but nevertheless observable in our measurements of $\Theta(f;t)$, particularly at frequencies encompassing a transition from leaky to trapped modes and in reduced contribution of higher order modes.

The residue associated with a given mode with horizontal wave number k_n is found upon evaluation of $(\partial/\partial p)(1+R_b e^{2i\gamma_n D})|_{p=k_n}$, where p is a member of the complex horizontal wavenumber plane. Here, the quantity $(\partial/\partial p)R_b|_{p=k_n}$ is necessarily evaluated numerically; note that Ellis and Chapman [9] provide a useful analytic solution to the residue evaluation, applicable to an elastic half-space but without the overlying elastic layer of thickness H.

Having established a residue contribution for each mode, for which we generally find approximately ten modes with varying trapped-to-leaky proportion depending on frequency, contour integration in the complex horizontal wave number plane is completed via the sum of these residue contributions. Note that the contribution associated with a Scholte wave or zeroth-order mode [9] is not evaluated because the frequency range is too high to observe such a contribution, and the surface ship excitation of a zeroth-order mode within this frequency range is not significant.

B. Adiabatic Construction of the Pressure and Particle Velocity Fields

The tidal mediated water depth at the IVAR location was 75.5 m during the 20-min observation period. The water depth for the source excitation, as represented by the changing position of *M/V Alice Oldendorf* (see Fig. 1), varied between 77 m (at CPA -10 min) and 79 m (at CPA $+10$ min). This depth was estimated by the AIS location of the vessel, combined with structure maps of two-way travel time measurements[1] for the seafloor and seabed horizons [10]. The change in depth between IVAR along any given transect connecting the two positions is assumed to be linear, as can be inferred in an approximate sense by Fig. 1. This assumption is verified at CPA by the two-way travel time to the seafloor for this transect parsed from the structure maps (see Fig. 4) showing reasonable agreement with a linear slope in the depth between the IVAR and ship positions.

Thus, we apply an adiabatic approximation, putting water depth at ship source location D^s, for example, equal to 78 m at CPA, with water depth at the fixed IVAR receiver location D^r equal to 75.5 m. Given the changing ship position, D^s varies

[1]Structure maps [10] are kindly provided by John Goff. Depth adjusted for tidal influence at the time of CPA.

in the data modeling used in the inversion, depending on the particular transect connecting the location of the vessel to that of the IVAR. The adiabatic approximation further assumes that the mud-layer depth H remains, at least on average, independent of this changing depth. This assumption is similarly supported by the two-way travel time data from the sea surface to the interface between the low-speed sediment layer and higher speed sediments (see Fig. 4, solid line), which follows a similar slope as the two-way travel time to the seafloor.

The complex acoustic pressure field as a function of frequency $P(f)$ for this combination of D^s and D^r is

$$P(f) = i\pi \sum_n N_n^s \sin(\gamma_n^s z^s) N_n^r \sin(\gamma_n^r z^r) H_0^{(1)}(\bar{k}_n R) \quad (7)$$

where $\bar{k}_n$ is the mean wave number in effect between depths D^s and D^r [11], and $H_0^{(1)}$ is the zeroth-order Hankel function of the first kind. The mode-dependent excitation coefficient is split into two parts to account for the difference in water depth at the source and receiver, where

$$N_n^r = \sqrt{4ik_n^r / \frac{\partial}{\partial p}(1 + R_b e^{2i\gamma_n^r D^r})|_{p=k_n^r}} \quad (8)$$

and where k_n^r and corresponding γ_n^r solve the characteristic equation governed by D^r. An analogous computation is made for N_n^s using k_n^s and γ_n^s established by the water depth at source D^s.

The sensor receiver depth z^r equals 74.25 m, or 1.25 m above the seabed on the IVAR platform. The source depth z^s is set to 5 m, because our experience with this setting is that source depths in the range 2–10 m yield the same modeling result as anticipated for a ship near-surface source. To find $\bar{k}_n$ for a given candidate seabed, we precompute k_n based on water depths between 75.5 and 79 m in 0.2-m steps. We do not have the depths between the vessel and IVAR for any given source–receiver propagation path, but the reasonably uniform bathymetric slope between these two points supports taking a simple, linear average between k_n found at a given D^s and that found at $D^r = 75.5$ m. Finally, optimization searches for range R is over a uniform search bound centered on the AIS range (i.e., prior information) for a given transect (see Section IV).

The complex horizontal $V_r(f)$ and vertical $V_z(f)$ particle velocity can now be computed as follows:

$$V_r(f) = \frac{1}{2f\rho_w} \sum_n \bar{k}_n N_n^s \sin(\gamma_n^s z^s) N_n^r \sin(\gamma_n^r z^r) H_1^{(1)}(\bar{k}_n R) \quad (9)$$

where $H_1^{(1)}$ is the first-order Hankel function of the first kind and ρ_w is the water density, and

$$V_z(f) = \frac{-1}{2f\rho_w} \sum_n \gamma_n^r N_n^s \sin(\gamma_n^s z^s) N_n^r \cos(\gamma_n^r z^r) H_0^{(1)}(\bar{k}_n R). \quad (10)$$

The complex pressure and particle velocities, each as a function of frequency for set range R, are assembled into a model for $\Theta(f)$ using

$$I_r(f) = \frac{1}{2}\mathrm{Re}\{P(f)V_r(f)^\star\} \quad (11)$$

and

$$I_z(f) = \frac{1}{2}\mathrm{Re}\{P(f)V_z(f)^\star\} \quad (12)$$

and a parallel construction using the imaginary part yields $Q_r(f)$ and $Q_z(f)$.

The quantities $I_{r,z}$, $Q_{r,z}$, and magnitudes are combined following (5) to yield a model $\Theta(f)$ computed in 1-Hz increments between 23 and 140 Hz, based on a given geoacoustic parameter vector $\mathbf{m}$ (discussed in Section IV), to establish a model vector $\mathbf{d}(\mathbf{m})$ representing a simulated replica of the data.

IV. Geoacoustic Inversion

As in our previous study [3], a geoacoustic inversion of the data is based within a Bayesian framework. In short, we seek the probability density function (PDF) $P(\mathbf{m}|\mathbf{d})$, an *a posteriori* probability density representing the PDF for model parameters $\mathbf{m}$ given the measured data vector $\mathbf{d}$ corresponding to estimates of circularity. This function equals the conditional PDF for the data given the model $P(\mathbf{d}|\mathbf{m})$, interpreted as a likelihood for $\mathbf{m}$ given that data $\mathbf{d}$ have been observed, multiplied by an *a priori* PDF for model parameters $P(\mathbf{m})$, assumed here to be a uniform distribution within the selected parameter bounds [12]–[14].

The experimental data vector $\mathbf{d}$ is represented by one time t segment of $\Theta(t; f)$ for frequencies 23–140 Hz every 1 Hz; upon removing the three interference frequency bins 86–88 Hz, length $\mathbf{d}$ equals 115. There are 241 such data vectors representing estimates of $\Theta(f; t)$ [one for each transect, e.g., as shown in Fig. 2(b) with time index ΔT of 5 s established in Section II] corresponding to the 20-min (1205-s) observation period, during which the vessel traveled approximately 5 km. Over the 241 separate inversions, we examine the slow variation in the inverted parameters as the vessel traversed the course (see Fig. 1).

Continuing with the example of the CPA transect [time index 0 of Fig. 2(b), and the red line in Fig. 1], we estimate a water depth of 78 m at the vessel location for this transect; using the adiabatic approach, all model vectors $\mathbf{d}(\mathbf{m})$ for this transect are generated on the basis of a linear change in depth between the 78-m water depth at the source (D^s) and the 75.5-m water depth at the receiver (D^r), where the depth change occurs over the nominal range of 2465 m given by the AIS. The AIS range to IVAR is prior information, and a relatively narrow search bound of $\pm$200 m about this value is used to invert for the final range. In our previous study [3], a much larger range-span for search bounds was evaluated and yielded excellent agreement between the inverted and AIS range using a nominal range-independent model for the seabed; here, given that finding range is a settled issue, the focus is on this range-dependent inversion for geoacoustic parameters.

The model space $\mathbf{m}$ contains four unknown parameters (see Table I), for which we assume uniform prior bounds and equidistant grid search space in each model dimension. To select search bounds for the first three parameters in Table I, we rely on previous results [3] in which median values of the maximum *a posteriori* (MAP) for estimates of c_{sed}, H_{sed}, and c_{base} over a subset of the observations within $\pm$10 min of CPA were 1478 m/s, 9.4 m, and 1800 m/s, respectively, and thus, our

TABLE I
UNKNOWN PARAMETERS IN MODEL SPACE $\mathbf{m}$ SHOWING SEARCH BOUNDS AND INCREMENT (MIDDLE VALUE), AND MEAN OF THE MAP VALUES OVER THE 241 TRANSECTS $\pm$ THE STANDARD DEVIATION

Parameter	Unit	Search Bounds	Mean Value, all Transects
H_{sed}	m	8.0 – 0.4 – 10.8	9.4 $\pm$ 0.3
c_{sed}	m/s	1450 – 6 – 1498	1470 $\pm$ 8
c_{base}	m/s	1725 – 25 –1875	1793 $\pm$ 14
v_{base}	m/s	25 – 60 – 625	350 $\pm$ 98

search bounds are nominally centered about these values. The inversion in the earlier study [3] utilized the absolute value of the relative phase between pressure and vertical particle velocity as the observable.

In this study, utilizing $\Theta(f;t)$ with full ± 1 variation, more nuanced properties are observed in the interference pattern, particularly at our lowest observable frequency range, motivating us to include shear effects in forward modeling and inversion. For example, Potty and Miller [15] evaluated the effect of shear on modal dispersion using broadband data from SBCEX2017, and estimate a shear speed of 410 m/s for what they refer to as the deep sediment layer, which corresponds to the basement half-space in our model [see Fig. 3(a)]. Our estimates of $v_{\rm base}$, here being allowed to vary smoothly as a function of transect, are shown to be nominally consistent with their estimate (see Section V).

The remainder of the model space consists of preset values because these parameters are unlikely to be further resolved with this set of underwater ship noise data, as confirmed by our experiment. Within the low-speed (mud) layer, sediment density $\rho_{\rm sed}$ is set to 1600 kg/m^3, representing the nominal value of the range observed in coring operations from SBCEX2017 [16]. Although our data appear to be insensitive to elastic properties within the low-speed layer, we nevertheless include the following parameters for completeness: a sediment shear speed $v_{\rm sed}$ of 25 m/s, also based on observations from the same site [17] (for which given the expected low sediment compressional speed puts the Poisson's ratio close to, but less than, the 0.5 bound for fluid media), and a sediment shear wave attenuation of 0.5 dB/λ, as informed by the large set of data published in [18, Fig. 5], for which this nominal value of attenuation maps to the low shear speed. Low-speed layer sediment compressional wave attenuation is $0.68 f_{\rm kHz}^2$ dB/m^{-1}, where $f_{\rm kHz}$ is the modeling frequency in kHz; this is based on an approximation[2] to viscous grain shearing theory [19], e.g., yielding $\sim$0.12 dB/λ at 120 Hz.

Within the basement half-space, the density $\rho_{\rm base}$ is tied to a given $c_{\rm base}$ value using an empirical fit of [21, Table IVA], translating to 1800–2000 kg/m^3 for the search bounds of $c_{\rm base}$ in our Table I. The basement compressional wave attenuation is set to 0.2 dB/λ, and the shear wave attenuation is set to 0.25 dB/λ, which are also informed by Bowles [18].

Key steps in the inversion process then follow from [12]; here, put the model–data mismatch column vector $\mathbf{r} = \mathbf{d} - \mathbf{d}(\mathbf{m})$ and find the data misfit function

$$E(\mathbf{m}) = \frac{N_f}{2} \log_e \mathbf{r}^T \mathbf{r}$$

with $N_f = 115$. There remains the assumption that data errors, as represented by $\mathbf{r}$, are Gaussian and uncorrelated [12], [13], and this assumption is addressed further in Section V.

The MAP values for the four geoacoustic parameters studied, including range, are considered the optimal estimates and are found by minimizing the $E(\mathbf{m})$ over the 5-D parameter space. Establishing $P(\mathbf{m}|\mathbf{d})$ follows, given that $P(\mathbf{m})$ is a uniform distribution in all dimensions, and 1-D marginal PDFs for the four geoacoustic model parameters along with range R are found upon summing the 5-D $P(\mathbf{m}|\mathbf{d})$ function over the appropriate model dimensions. As a measure of uncertainty for each parameter estimate, we compute the interval width containing 95% of the probability based on the corresponding 1-D marginal PDF [12].

V. RESULTS AND DISCUSSION

The inversion is completed for each of the 241 transects, i.e., using the 241 data vectors $\mathbf{d}$ [see Fig. 2(b)], with Table I providing an overall summary of results for the four geoacoustic parameters. Fig. 5 displays MAP values (magenta lines) for these parameters and 95% probability width (dashed, black lines) plotted as a function of longitude over the vessel's course (see Fig. 1), noting that vessel latitude is approximately constant over the 20-min period. The 95% probability width for sediment layer thickness $H_{\rm sed}$, and sediment and half-space compressional speeds $c_{\rm sed}$ and $c_{\rm base}$, with a few exceptions, reasonably bound the MAP values. For all parameters, the 95% probability width varies depending on transect, but representative values in the vicinity of the CPA are as follows: $H_{\rm sed}, \pm$ 0.5 m; $c_{\rm sed}, \pm$ 8.4 m/s; $c_{\rm base}, \pm$ 25 m/s; and $v_{\rm base}, \pm$ 146 m/s, with the 95% probability width for $c_{\rm base}$ approaching the increments in the grid search used in the inversion (see Table I). Estimates for the shear speed in the half-space $v_{\rm base}$ are, for some transects, encumbered by large uncertainties that press up against the search bounds (dotted, black lines), generally occurring when the MAP estimates are also very low. (When this occurs the MAP estimates [see Fig. 5(d)] are not displayed.)

A smoothed version of the results (see Fig. 5, cyan line) based on a 20-point (100 s) moving average, provides a sense of the slow variation in the average, effective seabed parameters that describe the seabed between the IVAR receiver and the ship source as the latter varies in longitude. The mean and standard deviation of the MAP values (see Table I) provide a single value that is nominally representative of the entire $\sim$5-km transit (see Fig. 1), and the moving average results are bound by this mean $\pm$ one standard deviation. Note that for $v_{\rm base}$ averaging excludes those estimates for which the 95% probability width spans the search bound, and the moving average is extended across data gaps. Taking the means and standard deviations

[2]Our approximation is of the particular attenuation curve generated by David Knobles, who incorporates sediment parameters for this model that apply to the low-speed, mud-like sediments studied in SBCEX2017.

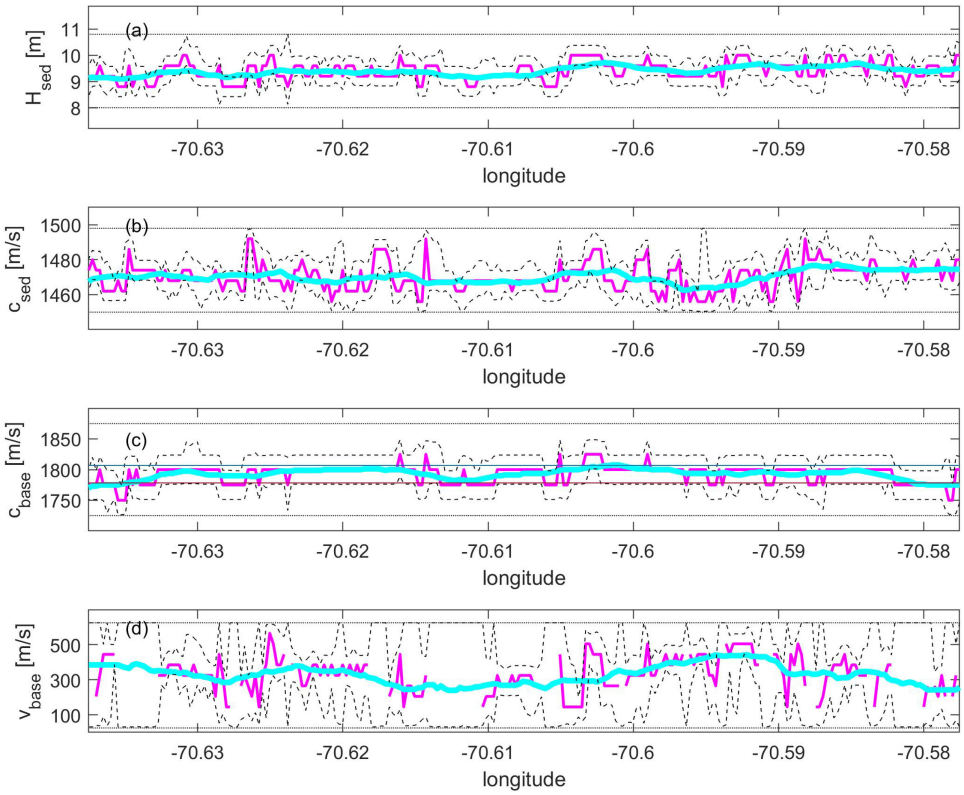

Fig. 5. Inversion results for the four geoacoustic variables given in Table I, plotted as a function of the longitude corresponding to the track of *M/V Alice Oldendorf* (see Fig. 1). (a) Low-speed sediment layer thickness $H_{\rm sed}$. (b) Sediment compressional speed $c_{\rm sed}$. (c) Half-space compressional speed $c_{\rm base}$. (d) Half-space shear speed $v_{\rm base}$. MAP values (magenta line) and 95% probability width (black, dotted line) are plotted along with a 20-point (or approximately 100 s) moving average (thick cyan line). Black dotted, horizontal lines depict the search bounds for each parameter. MAP estimates of shear speed $v_{\rm base}$ for which the probability width matches the search bound are excluded.

for $c_{\rm base}$ and $v_{\rm base}$ from Table I yields a Poisson's ratio for the sediment in the half-space over the transit of 0.48 ± 0.01, a value that is consistent with elastic properties of consolidated marine sandy sediments removed from the water–sediment interface [20].

The moving average results (see Fig. 5) are further used to construct a simulated replica of $\Theta(f;t)$ corresponding to the transit of the vessel within $\pm$ 10 min of CPA [see Fig. 2(c)]. That is, for each transect, the complex pressure and particle velocity field is computed as a function of frequency using the moving average of the inverted range for that transect (which agrees closely with the AIS range), plus the corresponding set of geoacoustic parameters emerging from the average, and the vessel source depth belonging to the transect. Using the moving average in this operation yields a more realistic simulation of $\Theta(f;t)$; i.e., the MAP values emerging from the inversion over each transect will differ slightly in a necessarily discrete manner.

Three examples of simulated $\Theta(f)$ generated by the specific MAP estimates for geoacoustic parameters and vessel range, corresponding to the inversion on data $\pm$500 s about the CPA and at CPA (see Fig. 6), compare well with the observations. As in the case of the complete simulated replica $\Theta(f;t)$ [see Fig. 2(c)], prior AIS information is used for the water depth at a given vessel location. For example, the water depth at the vessel location increases approximately 1 m between the two $\pm$500-s transects, where water depth at the CPA transect is $\sim$78 m.

The assumption concerning uncorrelated, Gaussian distributed residual errors is addressed with each transect, such as the three shown here. First, we find that the sample autocorrelation function of residual errors shows no effective correlation beyond 0-lag. A chi-square goodness-of-fit test is performed to evaluate the assumption that the residual errors are from a normal distribution, with significance level $p > 0.1$ for the examples shown in Fig. 6. However, for about 10% of the transects, p can fall below 0.05; for these few cases, the distribution of residual errors remains symmetric but tends to show heavier concentration near the mean (leptokurtic).

Our interpretation of some of the detailed, shallow water propagation effects manifested in these data is ongoing, though it is evident that the simulation reproduces observed circularity [see Fig. 2(c)] reasonably well. Going forward, a particularly interesting interpretive challenge is the circularity signal in the model result at 24 Hz [see Fig. 2(c)] at approximately $\pm$ 500 s and $\pm$ 200 s from CPA, relative to that at 23 Hz, for which there is a change in sign. The circularity data [see Fig. 2(b)] also show the same pattern at 24 Hz, but unfortunately the roll-off in ship noise radiation with decreasing frequency is fast here, with roll-off also apparent in the potential energy [see Fig. 2(a)]. However, we do know that the 23-to-24-Hz transition represents the onset of the

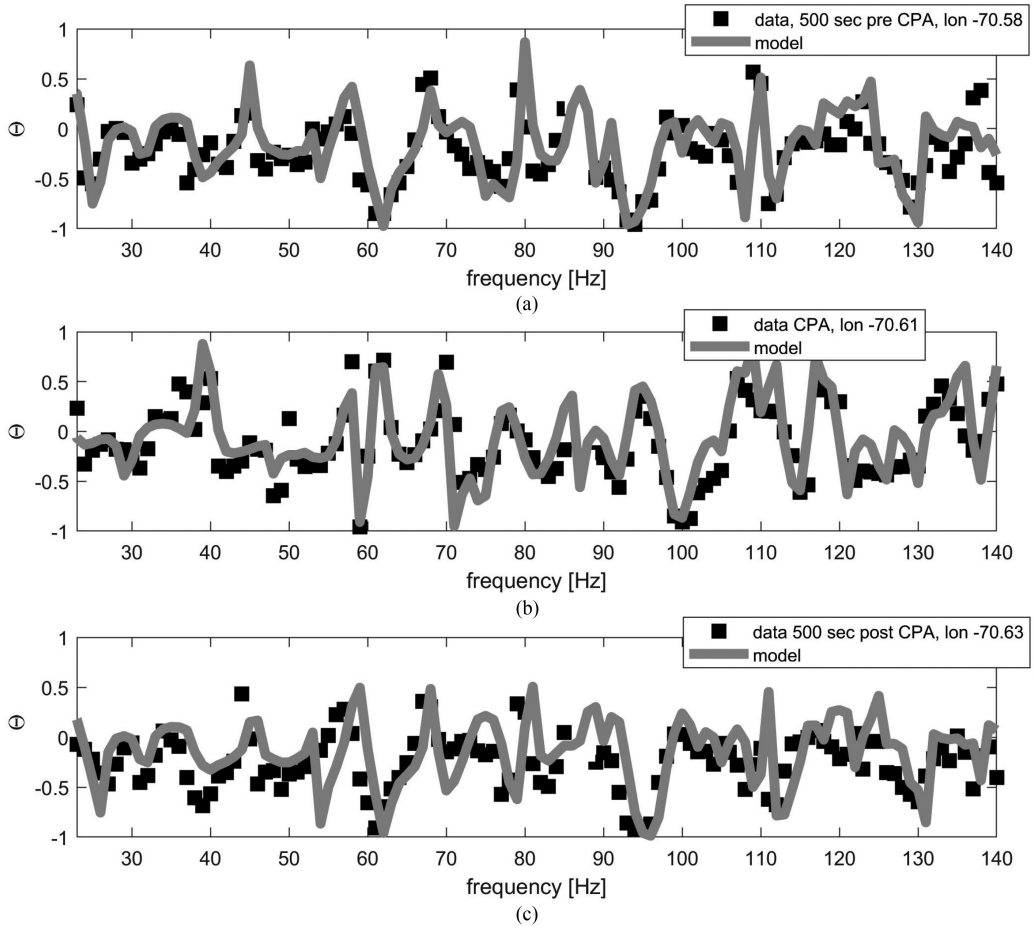

Fig. 6. (a) Estimate of circularity as a function of frequency $\Theta(f)$ for 23–140 Hz, generated by the specific MAP estimates for geoacoustic parameters and vessel range, corresponding to the inversion on data representing 500 s prior to CPA, at which time vessel longitude is -70.58. (b) $\Theta(f)$ generated by the MAP estimates at CPA, vessel longitude at -70.61. (c) $\Theta(f)$ generated by the MAP estimates 500 s post-CPA, vessel longitude at -70.63.

second mode, and this is expected to have a significant effect on circularity [2].

Also, it is possible to observe in the data [see Fig. 2(b)], although very faintly, a pattern in the circularity that is roughly confined to the region between 40 and 55 Hz and which emanates outward from CPA (time 0). This suggests the presence of a weak sound-speed gradient in the seabed, perhaps of order 1 s^{-1}, and the subsequent negative waveguide invariant, which is not captured in our current inversion scheme. Given the general weakness of this feature, our interpretation going forward will rely more on additional forward modeling rather than inversion.

The smoothed, inversion results suggest a kind of variation with longitude; for example, at the start of the observations, the sediment layer depth H_{sed} appears to be about 9.5 m, and this layer depth gradually thins to about 9.1 m near the end of the observations (viewed in an averaged sense). Although the influence of such variation on sound propagation as manifested in our data is subtle, evidence that this is a real effect comes from reconsidering the two-way travel time data first discussed in the context of Fig. 4. For each transect connecting the ship location to the IVAR location, an average sediment thickness is derived by taking the two-way travel time averaged over transect length, corrected for the first arrival to the seafloor. For example, for the CPA data in Fig. 4, this value is 12.264 ms, which yields a sediment thickness between 9.23 and 9.33 m, upon using the upper and lower bounds of the estimate for c_{sed} (see Table I). Applying this to all transects (see Fig. 7), the results are in reasonable agreement with the moving average inverted results H_{sed}, especially in a linear trend. Importantly, the adiabatic component of our analysis designed to accommodate the slowly changing water depth is essential to capture this trend. Finally, Goff *et al.* [10] and Belcourt *et al.* [22] refer to a transition layer of O(1) m between lower speed, mud-like sediment and the higher speed sandy sediment, the latter considered a half-space in our model, so some degree of ambiguity in delineating this boundary is expected.

The reasonably tight bounds about the parameter estimates for H_{sed}, c_{sed}, and c_{base} (see Fig. 5) point to the degree of sensitivity of the data to these properties. In contrast, the primary influence of parameter half-space shear speed v_{base} is on modal attenuation, as illustrated in Fig. 3(b), and it is reasonable to assume that the ability to measure this parameter is influenced by basic signal fluctuations, as evidenced in the potential energy spectrum [see Fig. 2(a)]. Nevertheless, although our overall average value of

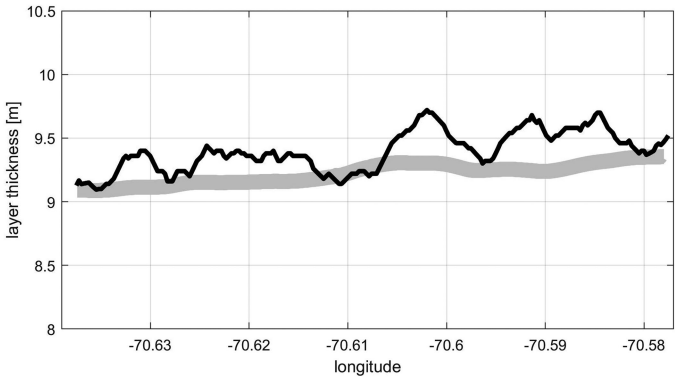

Fig. 7. Estimated thickness of the low-speed (mud) layer (black line) based on the smoothed results for $H_{\rm sed}$ [see Fig. 5(a)]. The gray line is derived from the two-way travel time averaged over each transect connecting the ship location to the IVAR location, based on the data from [10], where the thickness of the gray line maps to the upper and lower bounds of the estimate for $c_{\rm sed}$ (see Table I). Results are plotted as a function of changing longitude for the vessel track (see Fig. 1).

$v_{\rm base}$ is somewhat lower than the estimate of 410 m/s by Potty and Miller [15], we report several individual MAP estimates of $v_{\rm base}$ [see Fig. 5(d)] that are entirely consistent with their estimate. As for remaining geoacoustic parameterizations necessary to describe the low-speed, mud layer, i.e., sediment shear speed, and sediment shear wave and compressional wave attenuation, we reiterate that realistic fixed (or frequency-dependent) prior values are inserted into our model for completeness. Otherwise, these parameters are poorly resolved with our data.

VI. Conclusion

This article applies a Bayesian framework for the geoacoustic inversion of vector acoustic properties of the underwater noise from a cargo ship traversing the central region of the SBCEX2017, as measured using the IVAR platform deployed on the seabed at depth 75.5 m. The data are formulated into a measure known as circularity, a bounded, nondimensional quantity that is independent of the ship noise-source spectrum. Observations are made over a 20-min period during which the vessel traveled approximately 5 km east to west, with CPA about 2.5 km south of the IVAR position. The interpretative model used in the inversion process is based on the plane wave reflection coefficient for a layered, elastic seabed in conjunction with the depth-dependent Green's function, and small changes in water depth at the location of the ship source are addressed using adiabatic mode theory. The inversion results exhibit a slow variation (see Fig. 5) over the vessel's observed course, with mean results (see Table I). Given the basic areal geometry of inversion (see Fig. 1), these mean results notionally apply to an approximate seabed area of 7 km^2.

Acknowledgment

The vessel AIS information was provided by ONR, Code 32, Ocean Acoustics. The authors thank John Goff for sharing his stratigraphic data. Peter H. Dahl thanks Julien Bonnel for helpful discussions.

References

[1] P. S. Wilson, D. P. Knobles, and T. B. Neilsen, "Guest editorial: An overview of the seabed characterization experiment," *IEEE J. Ocean. Eng.*, vol. 45, no. 1, pp. 1–13, Jan. 2020.

[2] P. H. Dahl and D. R. Dall'Osto,"Vector acoustic analysis of time-separated modal arrivals from explosive sound sources during the 2017 seabed characterization experiment," *IEEE J. Ocean. Eng.*, vol. 45, no. 1, pp. 131–143, Jan. 2020.

[3] P. H. Dahl and D. R. Dall'Osto, "Estimation of seabed properties and range from vector acoustic observations of underwater ship noise," *J. Acoust. Soc. Amer.*, vol. 143, pp. EL345–EL350, 2020.

[4] D. R. Dall'Osto and P. H. Dahl, "Observations of water-column and bathymetric effects on the incident acoustic field associated with shallow water reverberation experiments," *IEEE J. Ocean. Eng.*, vol. 42, no. 4, pp. 1146–1161, Oct. 2017.

[5] D. R. Dall'Osto, P. H. Dahl, and J. W. Choi, "Properties of the acoustic intensity vector field in a shallow water waveguide," *J. Acoust. Soc. Amer.*, vol. 131, pp. 2023–2035, 2012.

[6] G. V. Frisk, *Ocean and Seabed Acoustics: A Theory of Wave Propagation*. Upper Saddle River, NJ, USA: Prentice-Hall, 1994, pp 186–193.

[7] P. J. Vidmar and T. L. Foreman, "A plane-wave reflection loss model including sediment rigidity," *J. Acoust. Soc. Amer.*, vol. 66, pp. 1830–1835, 1979.

[8] Z. Y. Zang and C. T. Tindle, "Complex effective depth of the ocean bottom," *J. Acoust. Soc. Amer.*, vol. 93, pp. 205–213, 1993.

[9] D. D. Ellis and D. M. F. Chapman, "A simple shallow water propagation model including shear wave effects," *J. Acoust. Soc. Amer.*, vol. 78, pp. 2087–2095, 1985.

[10] J. A. Goff, J. Chaytor, A. H. Reed, G. Gawarkiewicz, P. A. Wilson, and D. P. Knobles, "Stratigraphic analysis of a sediment pond within the New England Mud Patch: New constraints from high-resolution chirp acoustic reflection data," *Mar. Geol*. vol. 412, pp. 81–94, 2019.

[11] F. B. Jensen, W. A. Kuperman, M. B. Porter, and H. Schmidt, *Computational Ocean Acoustics*, 2nd ed. New York, NY, USA: Springer, 2011, p. 410.

[12] J. Bonnel, S. E. Dosso, and N. R. Chapman, "Bayesian geoacoustic inversion of single hydrophone light bulb data using warping dispersion analysis," *J. Acoust. Soc. Amer.*, vol. 134, pp. 102–130, 2013.

[13] R. Duan, N. R. Chapman, K. Yang, and Y. Ma, "Sequential inversion of model data for sound attenuation in sediment at the New Jersey Shelf," *J. Acoust. Soc. Amer.*, vol. 139, pp. 70–84, 2016.

[14] N. R. Chapman, "Perspectives on geoacoustic inversion of ocean bottom reflectivity data," *J. Mar. Sci. Eng.*, vol. 4, pp. 1–14, 2016

[15] G. R. Potty and J. H. Miller, "Effect of shear on modal arrival times," *IEEE J. Ocean. Eng.*, vol. 45, no. 1, pp. 103–115, Jan. 2020.

[16] M. S. Ballard *et al.*, "In situ measurements of compressional wave speed during gravity coring operations in the New England Mud Patch," *IEEE J. Ocean. Eng.*, vol. 45, no. 1, pp. 26–38, Jan. 2020.

[17] M. S. Ballard, K. M. Lee, A. R. McNeese, and P. W. Wilson, "Development of a system for in situ measurements of geoacoustic properties during sediment coring," in *Proc. 171st Meet. Acoust. Soc. Amer.*, May 2016, Art. no. 070001.

[18] F. A. Bowles, "Observations of attenuation and shear-wave velocity in fine-grained, marine sediments," *J. Acoust. Soc. Amer.*, vol. 101, pp. 3385–3397, 1997.

[19] M. J. Buckingham, "On pore-fluid viscosity and the wave properties of saturated granular materials including marine sediments," *J. Acoust. Soc. Amer.*, vol. 122, pp. 1486–1501, 2007.

[20] E. L. Hamilton, "Elastic properties of marine sediments," *J. GeoPhys. Res.*, vol. 76, pp. 579–604, 1971.

[21] E. L. Hamilton, "Geoacoustic modeling of the sea floor," *J. Acoust. Soc. Amer.*, vol. 68, pp. 1313–1340, 1980.

[22] J. Belcourt, C. W. Holland, S. E. Dosso, J. Dettmer, and J. A. Goff, "Depth-dependent geoacoustic inferences with dispersion at the New England Mud Patch via reflection coefficient inversion," *IEEE J. Ocean. Eng.*, vol. 45, no. 1, pp. 69–91, Jan. 2020.

Peter H. Dahl received the Ph.D. degree in ocean engineering from the Massachusetts Institute of Technology, Cambridge/Woods Hole Oceanographic Institution, Woods Hole, MA, USA, Joint Program in Oceanography and Oceanographic Engineering, in 1989.

He is currently a Senior Principal Engineer with the Applied Physics Laboratory, University of Washington, Seattle, WA, USA, and a Professor of Mechanical Engineering with the University of Washington. His research focus includes experimental and modeling studies on intensity vector acoustics, shipping noise, and the underwater sound field from explosive sources including the effects on aquatic life.

Dr. Dahl is a Fellow of the Acoustical Society of America (ASA). He was the Chair of the ASA Technical Committee on Underwater Acoustics, the ASA Executive Council, and ASA Vice President (2013–2014.)

David R. Dall'Osto received the Ph.D. degree in mechanical engineering from the University of Washington, Seattle, WA, USA, in 2013.

He is currently a Senior Research Scientist and Engineer with the Applied Physics Laboratory, University of Washington. His research focus includes modeling and measurement of acoustic intensity in the ocean and atmosphere, on both short-range and global scales. An important aspect of his research is the discovery of physical processes that produce structure in the intensity vector field, and validating such theoretical predictions through experiment.

REPORT DOCUMENTATION PAGE

Form Approved
OMB No. 0704-0188

1. REPORT DATE *(DD-MM-YYYY)*	**2. REPORT TYPE**	**3. DATES COVERED** *(From - To)*
26-08-2021	Final Technical	1/15/2017 - 4/14/2021

4. TITLE AND SUBTITLE
Intensity Vector Acoustics and Mid-Frequency Sonar Studies, and Experiment in Korean Coastal Waters

5a. CONTRACT NUMBER

5b. GRANT NUMBER
N00014-17-1-2170

5c. PROGRAM ELEMENT NUMBER

6. AUTHOR(S)
Peter Dahl

5d. PROJECT NUMBER

5e. TASK NUMBER

5f. WORK UNIT NUMBER

7. PERFORMING ORGANIZATION NAME(S) AND ADDRESS(ES)
University of Washington – Applied Physics Laboratory
4333 Brooklyn Avenue NE
Seattle, WA 98105-6613

8. PERFORMING ORGANIZATION REPORT NUMBER

9. SPONSORING / MONITORING AGENCY NAME(S) AND ADDRESS(ES)
Office of Naval Research (322)
875 North Randolph Street
Arlington, VA 22203-1995

10. SPONSOR/MONITOR'S ACRONYM(S)
ONR

11. SPONSOR/MONITOR'S REPORT NUMBER(S)

12. DISTRIBUTION / AVAILABILITY STATEMENT:
Distribution Statement A: Approved for public release; distribution is unlimited.

13. SUPPLEMENTARY NOTES

14. ABSTRACT
This report cover research completed between 15 January 2017 and 14 April 2021, funded by the ONR grant entitled: "Intensity Vector Acoustics and Mid-Frequency Sonar Studies Experimental in Korean Coastal Waters."
The objective was to increase our understanding of the acoustic intensity vector field as it applies to shallow water propagation and reverberation. A secondary objective involved two field experiments in Korea, one conducted in May 2017 with the second cancelled owing to COVID-19.
The start of this grant also overlapped with preparation and execution of the Seabed Characterization Experiment 2017 (SBCEX2017) experiment off New England in March 2017. Vector acoustic data emerging from SBCEX2017 was of extremely high quality relative to the Korea data, and thus the majority of effort from this grant was directed towards analysis of SBCEX2017 data.
Three works are included in this report and considered generally representative of the technical output of this grant. Two involve modeling and interpretation of vector acoustic observations using IVAR system during SBCEX2017. The third involves a study of 6-years of acoustic data obtained from the Regional Cabled Array site off the Oregon coast, revealing a subtle, but clearly discernable, influence of reduced shipping noise owing to the worldwide COVID-19 epidemic.

15. SUBJECT TERMS
Intensity vector, acoustic particle velocity, Seabed Characterization Experiment, IVAR, COVID-19

16. SECURITY CLASSIFICATION OF:			**17. LIMITATION OF ABSTRACT**	**18. NUMBER OF PAGES**	**19a. NAME OF RESPONSIBLE PERSON**
a. REPORT	**b. ABSTRACT**	**c. THIS PAGE**			Peter Dahl
Unclassified	Unclassified	Unclassified	UU	34	**19b. TELEPHONE NUMBER** *(include area code)* (206) 543-1300